



**AFRL-OSR-VA-TR-2013-0575**

**ULTRAFAST BEAM FILAMENTATION - SPATIO-TEMPORAL  
CHARACTERIZATION AND CONTROL**

**CHARLES DURFEE**

**TRUSTEES OF THE COLORADO SCHOOL OF MINES**

**11/01/2013  
Final Report**

**DISTRIBUTION A: Distribution approved for public release.**

**AIR FORCE RESEARCH LABORATORY  
AF OFFICE OF SCIENTIFIC RESEARCH (AFOSR)/RSE  
ARLINGTON, VIRGINIA 22203  
AIR FORCE MATERIEL COMMAND**

# REPORT DOCUMENTATION PAGE

Form Approved  
OMB No. 0704-0188

Public reporting burden for this collection of information is estimated to average 1 hour per response, including the time for reviewing instructions, searching existing data sources, gathering and maintaining the data needed, and completing and reviewing this collection of information. Send comments regarding this burden estimate or any other aspect of this collection of information, including suggestions for reducing this burden to Department of Defense, Washington Headquarters Services, Directorate for Information Operations and Reports (0704-0188), 1215 Jefferson Davis Highway, Suite 1204, Arlington, VA 22202-4302. Respondents should be aware that notwithstanding any other provision of law, no person shall be subject to any penalty for failing to comply with a collection of information if it does not display a currently valid OMB control number. **PLEASE DO NOT RETURN YOUR FORM TO THE ABOVE ADDRESS.**

<b>1. REPORT DATE (DD-MM-YYYY)</b> 31-10-2013		<b>2. REPORT TYPE</b> Final	<b>3. DATES COVERED (From - To)</b> Aug 2010 - Oct 2013		
<b>4. TITLE AND SUBTITLE</b> Ultrafast Beam Filamentation: spatio-temporal characterization and control			<b>5a. CONTRACT NUMBER</b> FA9550-10-1-0394		
			<b>5b. GRANT NUMBER</b> FA9550-10-1-0394		
			<b>5c. PROGRAM ELEMENT NUMBER</b>		
<b>6. AUTHOR(S)</b> Charles G. Durfee, Jeff A. Squier			<b>5d. PROJECT NUMBER</b>		
			<b>5e. TASK NUMBER</b>		
			<b>5f. WORK UNIT NUMBER</b>		
<b>7. PERFORMING ORGANIZATION NAME(S) AND ADDRESS(ES)</b> Colorado School of Mines, Department of Physics 1523 Illinois St. Golden, Co 80401			<b>8. PERFORMING ORGANIZATION REPORT NUMBER</b>		
<b>9. SPONSORING / MONITORING AGENCY NAME(S) AND ADDRESS(ES)</b> AF Office of Scientific Research 875 N. Randolph St Room 3112 Arlington, VA 22203			<b>10. SPONSOR/MONITOR'S ACRONYM(S)</b> USAF, AFRL		
			<b>11. SPONSOR/MONITOR'S REPORT NUMBER(S)</b>		
<b>12. DISTRIBUTION / AVAILABILITY STATEMENT</b>					
<b>13. SUPPLEMENTARY NOTES</b>					
<b>14. ABSTRACT</b> In this project, we studied the linear and nonlinear propagation of structured beams of ultrafast pulses. We have been taking advantage of the special characteristics of spatially-chirped beams, in which the frequency components cross each other at the focus of a lens. In this configuration, the pulse focuses temporally and spatially at the same time. We developed a theory for understanding the beam propagation, verified aspects of this theory experimentally, developed a suite of diagnostics to test the alignment of these beams. We also demonstrated application of these beams to cutting biological material. In the project we investigated the spatio-temporal properties of cross-polarized wave generation and its application to pulse characterization. We developed a four-wave mixing apparatus in which the spatial chirp and pulse front is controlled. We extended our knowledge of beam propagation to Bessel-Gauss beams, and developed a technique to produce a uniform axial line focus by shaping only the spatial phase of the starting beam. Finally, we showed for the first time that Kerr-lens modelocking can be achieved in a Ti:sapphire oscillator pumped only by laser diodes.					
<b>15. SUBJECT TERMS</b> Ultrafast Optics, filamentation, nonlinear beam					
<b>16. SECURITY CLASSIFICATION OF:</b>			<b>17. LIMITATION OF ABSTRACT</b>	<b>18. NUMBER OF PAGES</b>	<b>19a. NAME OF RESPONSIBLE PERSON</b>
<b>a. REPORT</b>	<b>b. ABSTRACT</b>	<b>c. THIS PAGE</b>			<b>19b. TELEPHONE NUMBER (include area code)</b>

# Ultrafast beam filamentation: spatio-temporal characterization and control

Final Report for Grant # FA9550-10-1-0394

Charles G. Durfee, [cdurfee@mines.edu](mailto:cdurfee@mines.edu), Jeff A. Squier, [jsquier@mines.edu](mailto:jsquier@mines.edu)  
Dept. of Physics, Colorado School of Mines, Golden, CO 80401

## **Abstract (200 word)**

In this project, we studied the linear and nonlinear propagation of structured beams of ultrafast pulses. We have been taking advantage of the special characteristics of spatially-chirped beams, in which the frequency components cross each other at the focus of a lens. In this configuration, the pulse focuses temporally and spatially at the same time. We developed a theory for understanding the beam propagation, verified aspects of this theory experimentally, developed a suite of diagnostics to test the alignment of these beams. We also demonstrated application of these beams to cutting biological material. In the project we investigated the spatio-temporal properties of cross-polarized wave generation and its application to pulse characterization. We developed a four-wave mixing apparatus in which the spatial chirp and pulse front is controlled. We extended our knowledge of beam propagation to Bessel-Gauss beams, and developed a technique to produce a uniform axial line focus by shaping only the spatial phase of the starting beam. Finally, we showed for the first time that Kerr-lens modelocking can be achieved in a Ti:sapphire oscillator pumped only by laser diodes.

## **Executive summary of results:**

### **1. SSTF theory: Intuitive Analysis of Space-time Focusing with Double-ABCD Calculation**

- We developed an analytic and intuitive approach to calculate the spatio-temporal propagation of wide bandwidth pulses that have spatial chirp. In this approach, each frequency component can be propagate through an optical system using Gaussian ABCD matrices, while the central beam axes of the components is traced through the system with geometric optics. The technique provides useful insight into how space-time focusing occurs as well as how these beams can be controlled to control spatio-temporal propagation.
- In collaboration with Ya Cheng at the State Key Laboratory of High Field Laser Physics, Shanghai Institute of Optics and Fine Mechanics, we showed experimentally and theoretically that the peak intensity distribution for a focused spatially chirped pulse is tilted. This new tilt is qualitatively distinct from the pulse front tilt.
- Method is described in detail in a 16 page paper (Optics Express, 2012) and in an invited book chapter (Nova Science, 2013). A talk contributed to CLEO 2012 was one of a small number of talks that was upgraded to an invited talk.

### **2. SSTF experiment: Highly Localized Plasma Formation in Air Using Space-time Focusing of mJ Ultrafast Pulses**

- We developed a high-power spatial-chirp focusing experiment and demonstrated that a beam with 5 times the critical power for self-focusing can propagate to a focal point without distortion.
- Presented at CLEO, Advanced Photonics and a local conference.

**3. *SSTF application: Tissue ablation***

- Demonstrated extreme localization of tissue cutting using SSTF, with a porcine eye lens as the target. SSTF showed much more precise cutting and lower collateral damage than a conventional focus.
- Paper in Biomedical Optics Express (2013). Presented at Photonics West and in an invited talk in Corsica, France (2013).

**4. *SSTF characterization: Passive dispersion scan, Broadband beamlet scan, and Broadband shearing interferometry***

- We have developed three techniques to characterize broadband, spatially-chirped beams. All three of these have been demonstrated experimentally, and we are in the process of finalizing the analysis for publication.
- The passive dispersion scan takes advantage of the geometric spectral phase that results from an angular spatial chirp predicted by our theory. The spectrum of the second harmonic is monitored as the doubling crystal is moved along the optical axis. This movement effectively changes the second order phase on the pulse, producing an image that traces out the second derivative of the spectral phase intrinsic to the pulse.
- The broadband beamlet scan is a spectrally resolved knife-edge scan, that will give the beamlet axis direction, the location of the waist, and the size of the waist. Since all spectral components of the spatially-chirped beam are scanned at once, this measurement gives the complete description of the spatial characteristics of the spatially-chirped beam.
- Broadband shearing interferometry uses a Sagnac interferometer to produce a spatial shear (transverse displacement) and a birefringent plate to give a time delay. The resulting interferogram in an imaging spectrometer yields a measurement of the divergence angle as a function of frequency. We are working to extend this technique to make a self-referenced spatial wavefront measurement and a measurement to characterize angular spatial chirp.

**5. *Characterization: Development of a passively stable interferometric transient grating apparatus to characterize nonlinear dynamics***

- With an aim towards developing plasma diagnostics our MS student developed a passively stable optical arrangement for interferometric transient grating measurements.
- Presented at two local conferences.

**6. *Pulse characterization and energy contrast measurement using crossed-polarized wave generation (XPW) and self-referenced spectral interferometry***

- We developed a method to use XPW and spectral interferometry to quantify the energy contrast of laser pulses, an important issue in spectral interferometry and any experiments with linear pulse interactions.
- Presented at CLEO 2011, manuscript in preparation.

**7. *Efficiency enhancement of crossed-polarized wave conversion of low energy pulses via imaged double-pass***

- We showed that the spatio-spectral phase of cross-polarized wave (XPW) generated light can be controlled through re-imaging so as to improve double-pass XPW conversion. This will have applications to pulse shortening and contrast cleaning, especially for pulses from fiber amplifiers which are known for developing nonlinear distortion.
- Presented at CLEO 2012, manuscript in preparation.

#### **8. Pulse delivery to a uniform line focus with shaped Bessel-Gauss beams**

- We developed a technique to shape the spatial phase of a Bessel-Gauss ring beam to produce an on-axis line focus with a desired intensity profile. This was a collaboration with J. Gemmer and J. Moloney at U. Arizona.
- Two papers in 2013 (one still in review)

#### **9. Direct Diode Pumped Kerr Lens Modelocked Ti:Sapphire Laser Oscillator**

- We developed the first Kerr Lens modelocked Ti:sapphire laser that is directly pumped by laser diodes. We employed two blue laser diodes (450nm), focused into a modified Ti:sapphire laser.
- Published in Optics Express and featured on the cover of Laser Focus World. Presented at CLEO 2012, Ultrafast Phenomena 2012, Frontiers in Optics 2012.

#### **Students supported:**

Marin Iliev (PhD, anticipated graduation Spring 2014)

Michael Greco (PhD, anticipated graduation, Spring 2015)

Benjamin Galloway (MS, graduated Spring 2012, now a PhD student in the Kapteyn/Murnane group at U. Colorado).

#### **Honors:**

In 2013, C. Durfee was elected as a Fellow of the Optical Society of America

#### **Invited talks and seminars:**

J. Squier, E. Block, M. Greco, A. Allende Motz, C. Durfee, O. Masihzadeh, D. Ammar, M. Kahook, N. Mandava, “Simultaneous spatio-temporal focusing for tissue manipulation, “ **invited talk**, Progress in Ultrafast Laser Modifications of Materials, Cargese, Corsica, April 14-19, 2013.

C. Durfee, M. Greco, A. Meier, E. Block, J. Squier, “Spatial chirp control of high intensity 4D pulse focusing for laser-matter interactions,” **invited talk**, Progress in Ultrafast Laser Modifications of Materials, Cargese, Corsica, April 14-19, 2013.

J. Squier, “Inexpensive femtosecond laser sources and precise targeted ablation using simultaneous spatial and temporal focusing, “ **invited talk**, Frontiers and Challenges in Laser-Based Biological Microscopy, Telluride, CO, August 5-9, 2013.

C. G. Durfee, J. A. Squier, M. Greco, B. Galloway, A. Meier, E. Block, “Control of ultrafast laser-matter interactions with 4D pulse focusing,” **invited talk** Physics of Quantum Electronics (PQE), Snowbird, UT (Jan 2013).

“Linear and Nonlinear Dynamics of Focusing Spatially-Chirped Ultrafast Pulses,” Michael Greco, Amanda Meier, Erica Block, Dawn Vitek and Jeff A. Squier, **invited talk** COFIL, Tuscon, AZ (2012).

J. Squier, “Multifocal multiphoton imaging and micromachining with spatial and temporal focusing,” **invited talk** 8845-3, SPIE Optical Engineering and Applications, San Diego, CA,

Durfee, C., Squier, J. A., Meier, A., Iliev, M., Greco, M., Block, E., & Vitek, D. N. *Characterizing and controlling the spatial and temporal evolution of ultrafast laser pulses. Seminar, University of Colorado.* Boulder, Colorado (March, 2012).

Durfee, C., Greco, M., Block, E., Vitek, D. N., & Squier, J. A., “Intuitive analysis of space-time focusing with double ABCD calculation,” **contributed upgraded to invited talk**, *Conference on Lasers and Electro-Optics (CLEO)*. San Jose, CA (May 8, 2012).

Jeff Squier, Dawn Vitek, Erica Block, Michael Young, Charles Durfee, "Femtosecond micromachining using spatio-temporal focusing," **invited talk**, Optomechatronics Conference, Hong Kong, China, November 1-3, 2011

Jeff Squier, Dawn Vitek, Erica Block, Michael Young, Charles Durfee, "Femtosecond micromachining using spatio-temporal focusing," **invited talk**, Ultrafast Optics Conference, Monterey, CA, Sept. 26-30, 2011

### **Contributed talks and posters:**

“Ultrafast dynamics of 4D focusing of spatially-chirped pulses,” C. G. Durfee, M. Greco, E. Block, J. A. Squier. Ultrafast Optics, Davos Switzerland (March 2013).

“*Passively aligned four-wave mixing apparatus for investigating high-intensity laser-matter interactions*”, A. Meier, M. Greco, J. Thomas, J. A. Squier, C. G. Durfee. Photonics West (Feb 2013).

“*Highly localized plasma formation in air using space-time focusing of mJ ultrafast pulses*,” M. Greco, J. A. Squier, C.G. Durfee, at Conference on Earth Energy Research (Golden, March 2012).

“*Passively stable and dispersion compensated transient grating apparatus to measure ultrafast dynamics*,” B. Galloway, C.G. Durfee, at Colorado School of Mines colloquium (Golden, April 2012).

“Two photon microscope based on direct diode pumped Ti:sapphire laser,” Jeff A. Squier, Michael Young, Tristan Storz, Jonathan Garlick, Steven Hill, Matt Kirchner, Greg Taft, Kevin Shea, Henry Kapteyn, Margaret Murnane, Charles Durfee III, and Sterling Backus, Ultrafast Phenomena, Geneva, Switzerland, July 2012.

“Kerr-Lens Modelocked Ti:Sapphire Laser Oscillator Directly Pumped with Blue Diodes,” Charles G. Durfee, Tristan Storz, Jonathan Garlick, Steven Hill, Jeff A. Squier, Matt Kirchner, Greg Taft, Kevin Shea, Henry Kapteyn, Margaret Murnane, and Sterling Backus, Frontiers in

Optics, Rochester, NY (2012).

C. G. Durfee, T. Storz, J. Garlick, S. Hill, J. A. Squier, M. Kirchner, G. Taft, K. Shea, H. Kapteyn, M. Murnane, and S. Backus, "Direct diode pumped Kerr lens modelocked Ti:Sapphire laser oscillator," CM2J, 1–2 Conference on Lasers and Electro-Optics (CLEO) (2012).

Greco, M., Meier, A., Block, E., Vitek, D. N., Squier, J. A., & Durfee, C. G., *Highly localized plasma formation in air using space-time focusing of mJ ultrafast pulses. Advanced Solid State Photonics*. Colorado Springs, CO (June 17, 2012).

Galloway, B., & Durfee, C. G., Passively stable and dispersion compensated transient grating apparatus to measure ultrafast dynamics. *Optical Society of America, Rocky Mountain Section*. Boulder, CO (2012, April 19).

M. Greco, A. K. Meier, E. Block, M. Iliev, D. N. Vitek, J. A. Squier, C. G. Durfee, "Highly localized plasma formation in air using space-time focusing of mJ ultrafast pulses," JW4A, 1–2 Conference on Lasers and Electro-Optics (CLEO) (2012).

M. Iliev, A. K. Meier, C. G. Durfee, "Improvement of double-pass crossed-polarized wave efficiency and beam quality via imaging," JTh2A, 1–2 Conference on Lasers and Electro-Optics (CLEO) (2012).

"Measurement of Energy Contrast of Amplified Ultrashort Pulses using Cross Polarized Wave Generation and Spectral Interferometry," M. Iliev, A. K. Meier, D. E. Adams, J. A. Squier, and C. G. Durfee, in CLEO:2011 - Laser Applications to Photonic Applications, OSA Technical Digest (CD) (Optical Society of America, 2011), paper CTuO2.

"Spatio-temporally Focused Femtosecond Laser Pulses for Anisotropic Writing in Optically Transparent Materials," D. N. Vitek, Erica Block, Yves Bellouard, Daniel E. Adams, Sterling Backus, David Kleinfeld, Charles G. Durfee, and Jeff A. Squier. Conference on Lasers and Electro-Optics (CLEO), OSA Technical Digest (CD) (Optical Society of America, 2011), paper CWO5.

### **Refereed journal articles:**

C.G. Durfee, T. Storz, J. Garlick, S. Hill, J. A. Squier, M. Kirchner, G. Taft, K. Shea, H. Kapteyn, M. Murnane, and S. Backus, "Direct diode-pumped Kerr-lens mode-locked laser", *Opt Express*, **20**, 13677 (2012).

Durfee, C. G., Greco, M., Block, E., Vitek, D., & Squier, J. A. "Intuitive analysis of space-time focusing with double-ABCD calculation." *Optics Express*, **20**, 14244 (2012).

Benjamin Galloway, "Development of a passively stable and dispersion compensated transient grating apparatus to measure ultrafast dynamics" M.S. Thesis, Applied Physics, Colorado School of Mines, May 2012.

Charles G. Durfee, Michael Greco, Erica Block, Dawn Vitek, and Jeff A. Squier, "Intuitive Analysis Of Ultrafast Pulse Propagation Through Angularly Dispersive Structures," **invited book chapter** New Developments in Photon and Materials Research, ed. J. I. Jang (NOVA

Science, 2013).

E. Block, M. Greco, D. Vitek, O. Masihzadeh, D. A. Ammar, M. Y. Kahook, N. Mandava, C. Durfee, and J. Squier, "Simultaneous spatial and temporal focusing for tissue ablation," *Biomed. Opt. Express*, vol. 4, no. 6, p. 831, 2013.

C. G. Durfee, J. Gemmer, and J. V. Moloney, "Phase-only shaping algorithm for Gaussian-apodized Bessel beams," *Opt Express*, vol. 21, no. 13, p. 15777, 2013.

J. A. Gemmer, S. C. Venkataramani, C. G. Durfee, and J. V. Moloney, "Optical beam shaping and diffraction free waves: a variational approach," *arXiv.org*, vol. math.OA. 23-Jul-2013.

Fei He, Bin Zeng, Wei Chu, Jielei Ni, Koji Sujioka, Ya Cheng, and Charles G. Durfee, "Characterization and control of peak intensity distribution at the focus of a spatiotemporally focused femtosecond laser beam," *to be submitted to Optics Express* (2013).

#### **Nonrefereed articles:**

"Pumping of Ti:sapphire moves to the blue," C. Wood, S. Backus, J. Squier, C. Durfee, *Laser Focus World*, 9/01/2012 (**Cover article**).

### **Project Details**

#### ***1. SSTF theory: Intuitive Analysis of Space-time Focusing with Double-ABCD Calculation***

During this reporting period, one of the major accomplishments was to develop a solid theoretical understanding of the propagation of spatially-chirped beams and to confirm aspects of the theory experimentally[1], [2]. The work with simultaneous spatial and temporal focusing (SSTF) has broad applications to any area where a high peak intensity pulse must be delivered to a target area without nonlinear distortion. We have previously demonstrated the applications to micromachining, where an ultrashort pulse can be focused through a transparent medium on the way to the surface to be machined. This year (supported by another funded project) we demonstrated that SSTF can be used in laser eye surgery applications to provide greater precision in cuts with much lower collateral damage. We are also working to apply the SSTF technique to the controlled long-range atmospheric propagation of intense pulses. This promises to have applications to remote sensing and the creation of plasma structure that can guide or direct microwave pulses through the air.

In this project, we analyze the structure of space-time focusing of spatially-chirped pulses using a technique where each frequency component of the beam follows its own Gaussian beamlet that in turn travels as a ray through the system. Typically, spatial and angular chirp in ultrafast optical systems is avoided, but recent work in nonlinear microscopy and micromachining has taken advantage of the special properties of these beams. When a beam that has transverse spatial chirp is focused with a lens or curved mirror (see Fig 1a), the axial intensity is strongly localized because the pulse duration is not its shortest until all frequency components are fully overlapped. The strong localization that results from this simultaneous space-time focusing (SSTF) is useful for multiphoton microscopy because it improves the axial resolution. In micromachining, we have shown that it strongly suppresses nonlinear propagation

in a medium along the way to the focus, allowing machining on the back side of a transparent medium or on a surface immersed in water. The spatio-temporal structure of these pulses is quite interesting: there is a strong pulse front tilt at the focus (which appears to be responsible for the nonreciprocal writing effect), and adjustment of the input spectral chirp can move the focus in the axial direction.

The detailed spatio-temporal structure of these beams can be calculated directly with Fresnel propagation. However, it is difficult to interpret the analytic form of the results and to generalize to other systems. In this project, we developed a flexible, intuitive technique, the double ABCD method, that allows us to analyze and design spatially-chirped propagation systems. The propagation of the central axes of the Gaussian beamlets are first propagated as rays, either with paraxial ABCD matrices or non-paraxial tracing, (Fig 1b). The second step is to propagate the Gaussian beamlets through the system as if they are traveling along the optical axis (Fig 1c). Finally, the ray angles calculated from the raytrace are used to modify the expression for the Gaussian beam, thereby incorporating the phase information correctly. This method can accurately describe the spatio-temporal structure of propagating beams with spatial chirp.

To illustrate the insight that emerges from this analysis, we can calculate the different contributions to the axial localization for this focused spatially chirped beam (Fig 2a). A given Gaussian beamlet has the axial intensity distribution shown with the dashed line. Since the beam is spatially chirped, some intensity localization results from the higher numerical aperture in the chirped direction (black, solid). If the pulse duration were limited by the local bandwidth, the profile would be narrower (blue), but not as narrow as the full calculation shows (red). The

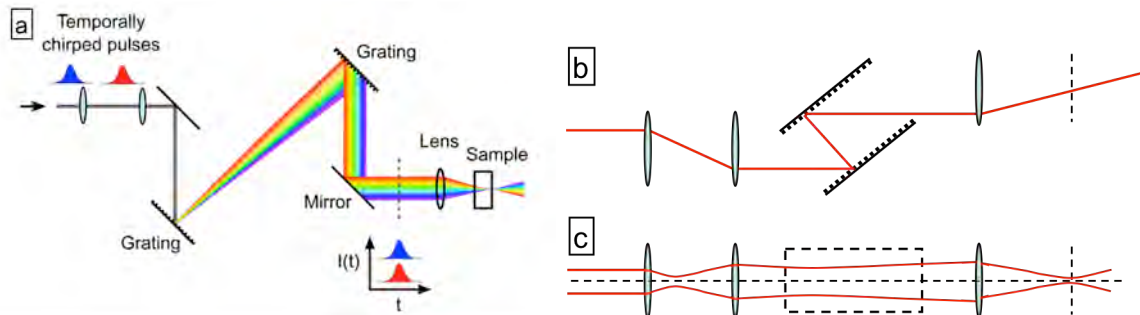


Figure 1. (a) An optical arrangement for space-time focusing comprised of a single-pass grating compressor. Each spectral component travels through the system as a Gaussian beamlet. The axis of the beamlet is traced as a ray (b) and as an on-axis Gaussian beam. The spectral dependence of the position and angle of a beamlet is incorporated into the description of the Gaussian beam, resulting in a complete description of the spatio-spectral wave.

remaining localization comes from a spectral chirp that is present within the confocal parameter of the focus (discussed below). The degree of localization increases with the spatial chirp aspect ratio: in fact it is possible to obtain a nearly spherical focal volume (Fig. 2b).

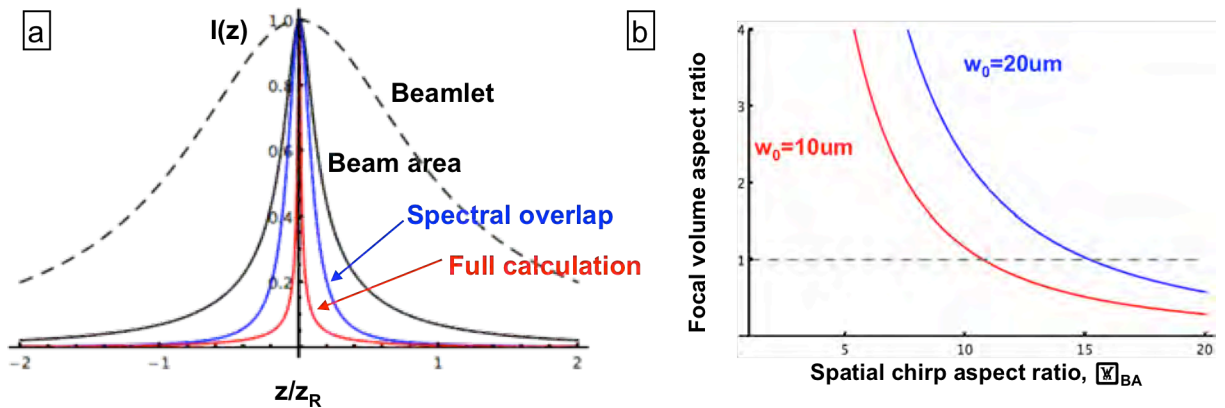


Figure 2. (a) Contributions to the axial confinement of a space-time focused beam. (b) Aspect ratio of the axial to the transverse width of the focal volume as the degree of spatial chirp is increased. Dashed line indicates an approximately spherical focal volume.

The calculated expressions contain the information on the wavefronts of the individual Gaussian beamlets (information not available in a direct Fresnel calculation). By examining the evolution of the wavefronts as the beamlets move through the focus, the origin of the axial dependence of the spectral chirp becomes clear (Fig. 3). At the focus, the individual wavefronts are flat and there is no chirp there. As the beams move through the Rayleigh range, the wavefront curvature develops, and variation in the on axis phase can be seen. This variation in phase is in fact predominately parabolic in frequency, resulting in a pulse chirp that reaches a maximum at one Rayleigh length from the focus. At large distance, the wavefronts all overlap, and the chirp disappears. On the other side of the focal plane, the chirp has the opposite sign. This approach gives insight into how misalignment of the system affects the localization and provides a means to design optical systems that make use of spatially-chirped beams. Along with the theoretical basis of this approach, we compare below our predictions with our experimental measurements of breakdown in air, which show good agreement.

In collaboration with a group in Shanghai (State Key Laboratory of High Field Laser Physics, Shanghai Institute of Optics and Fine Mechanics), we investigated some of the

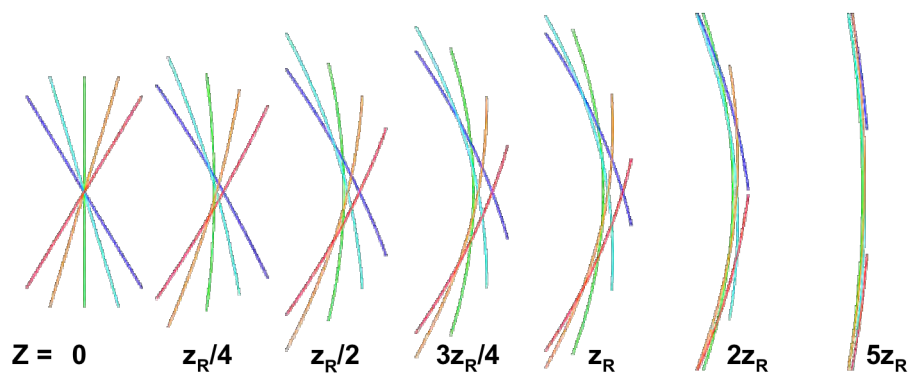


Figure 3. Evolution of the wavefronts in a focused spatially-chirped beam.  $z_R$  is the Rayleigh range of a Gaussian beamlet. The on-axis wavefront shows the geometric origin of the frequency chirp at either side of the focal plane.

interesting and important properties of SSTF focused beams. The Chinese group made measurements of two-photon fluorescence excitation (TPFE) at the focus of a spatially chirped

femtosecond laser beam that revealed an unexpected tilted peak intensity distribution in the focal spot. The CSM theoretical calculation showed that the tilting of the peak intensity distribution originates from the fact that along the optical axis of objective lens, the spatiotemporally focused pulse reaches its shortest duration exactly at the focal plane. However, when moving away from the optical axis along the direction of spatial chirp of the incident pulse, the pulse reaches its shortest duration either before or after the focal plane, depending on whether the pulse duration is measured above or below the optical axis as well as the sign of the spatial chirp. The tilting of the peak intensity distribution in the focal spot of the spatiotemporally focused femtosecond laser beam can play important roles in applications such as femtosecond laser micromachining and bio-imaging.

In this report, we will concentrate on the theoretical analysis contributed by the CSM group. The pulse front tilt (PFT), the dependence of the arrival time of the pulse on the transverse coordinate, is controlled by the combination of angular or lateral spatial chirp with spectral chirp[1]. In the present case of the spatio-temporal focusing, the temporal chirp is precompensated and  $\phi_2 = 0$ , the PFT is introduced by the angular dispersion alone. In our experiment the pulse is spatially chirped in the transverse direction before the lens, and the lens converts this transverse spatial chirp to angular chirp. The Gaussian beam can be written in terms of the amplitude and phase as

$$E(x, y, z, \omega) = A(x, y, z, \omega) \exp [i\phi(x, y, z, \omega)]. \quad (1)$$

Following the analysis in our paper[1], we can treat a particular frequency component as an individual beamlet. After focusing by the lens, the amplitude function for the beamlet propagating at a frequency-dependent angle  $\theta_x$  can be written

$$A(x, y, z, \omega) = A(\omega) \frac{w_0}{w(z)} \exp \left[ -\frac{(x - z \sin \theta_x)^2 + y^2}{w^2(z)} \right] \quad (2)$$

and the phase function, under the paraxial approximation can be written as

$$\phi(x, y, z, \omega) = k_0 x \sin \theta_x + k_0 z \left( 1 - \frac{1}{2} \sin^2 \theta_x \right) - \eta(z) + k_0 \frac{(x - z \sin \theta_x)^2 + y^2}{2R(z)}, \quad (3)$$

where  $k_0$  is central wave vector of the pulses,  $R(z)$  is the radius of the curvature of the beam's wavefront and  $\eta(z)$  is the Gouy phase shift. We define the frequency dependence of the beamlet angle as

$$\sin \theta_x \approx \theta_x = \alpha(\omega - \omega_0) / f. \quad (4)$$

For future reference the spatial chirp rate is related to the angular chirp rate  $\alpha$  through

$$\beta = \alpha \Delta \omega / w_{in}. \quad (5)$$

When the spectral phase is expanded to second order we can obtain the spatial dependence of the pulse chirp[1]:

$$\phi_2(x, z) = \left( \frac{x}{w_0} \frac{\tau_0 \beta}{\omega_0} - \frac{z}{z_R} \frac{\tau_0^2 \beta^2}{4} \right) \left( \frac{1}{1 + z^2 / z_R^2} \right), \quad (6)$$

where  $\tau_0 = 2 / \Delta \omega$  is the transform limited pulse duration. This spectral phase originates from the evolution of the wavefront curvature of each of the beamlets. It is evident in this expression that there is a line in the x-z plane where this geometric phase is zero. Solving for where  $\phi_2 = 0$  we can get

$$z(x) = \frac{2}{\beta} \frac{x}{w_0} \frac{\Delta \omega}{\omega_0} z_R, \quad (7)$$

where we have used Eq. 5 for the spatial chirp rate  $\beta$ , the focal spot size is  $w_0 = \lambda f / \pi w_{in}$ , and the beamlet Rayleigh range is  $z_R = \pi w_0^2 / \lambda$ . We can also get:

$$z(x) = \frac{2f}{\alpha\omega_0} x . \quad (8)$$

Thus the value of the IPT angle  $\theta_t$  can be evaluated as:

$$\tan \theta_t = \frac{\alpha\omega_0}{2f} . \quad (9)$$

Intuitively, the slope of IPT is proportional to the angular chirp rate and inverse proportional to the focal length of the lens.

From Eq. (9), it is clear that the pulse duration will be at a minimum along a plane that is tilted with respect to the  $z$  axis. This intensity plane tilt (IPT) is distinct from what is called the pulse front tilt (PFT), which describes the arrival time of the pulse across the beam for a fixed value of  $z$ .

For any amount of angular spatial chirp, the IPT will be present, but whether the effect will be noticeable is not obvious from the expression. Since spatio-temporal focusing confines the axial intensity profile compared to the Rayleigh range of the beamlet, we can compare the axial *shift* in  $X$  at the beam radius to the axial *width* (the depth of focus). In the limit of large spatial chirp rate, we can obtain an approximate expression for  $z_{DOF}$ , the axial full-width at half-maximum (FWHM) from the analytic expression for the axial intensity profile (Eq. (31) in [1]).  $z_{DOF}$  can be expressed in the simple form

$$z_{DOF} \approx \frac{\sqrt{3}}{1+\beta^2} z_R . \quad (10)$$

Calculating the ratio in the limit  $\beta^2 \gg 1$ , we find that

$$\frac{z(x)}{z_{DOF}} \approx \frac{2}{\sqrt{3}} \beta \frac{x}{w_0} \frac{\Delta\omega}{\omega_0} = \frac{1}{\sqrt{3}c} \frac{\alpha\Delta\omega^2}{f} x . \quad (11)$$

From this expression we can see that at  $x = w_0$ , the IPT will result in a  $z$ -shift  $\delta z$  that can be comparable to  $z_{DOF}$  for spatial chirp rate sufficiently large that  $\beta\Delta\omega/\omega_0$ . This relative IPT is actually independent of the focusing conditions ( $f$  and  $w_0$ ), and solely dependent on the spatial chirp rate and the fractional bandwidth.

It is instructive to compare the IPT to the PFT. The PFT, *i.e.* the tilt in  $x$ - $t$  in the focal plane arises from the calculation of the variation of the group delay with position. At  $z=0$ , we can write

$$\phi_1(x) = \frac{\alpha\omega_0}{cf} x = \frac{\beta\tau_0}{w_0} x \quad (12)$$

where, as in Ref [1], we have used Eq. (8),  $\tau_0 \Delta\omega = 2$ , and  $w_0 = 2cf/\omega_0 w_{in}$  to simplify the expression. The temporal shift of the pulse at the spot radius is  $\beta\tau_0$ . For positions  $x > 0$  in the focal region, the pulse arrives later (larger group delay) and the  $z$  position of maximum intensity is farther from the lens ( $z > 0$ ). Figure 4 illustrates the relative orientations of the tilt in the peak intensity plane in the  $XZ$  plane.

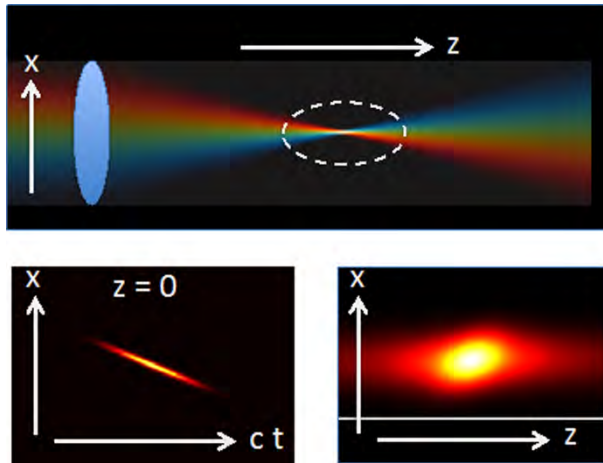


Fig 4. Illustration of the relative orientations of the spatial chirp (top), pulse front tilt (lower left), and intensity plane tilt (lower right). The PFT is represented as a snapshot so that the leading edge of the pulse is at larger  $z = ct$ .

## ***2. SSTF Experiment: Highly Localized Plasma Formation in Air Using Space-time Focusing of mJ Ultrafast Pulses***

Space-time focusing of spatially-chirped Ti:Sapphire laser pulses is used to generate a plasma in air axially localized to 28x less than the confocal parameter, suppressing filamentation on the way to the focus. In high-intensity interaction of lasers with matter, nonlinear propagation through a medium on the way to the target has long been a serious issue. Ionization defocusing and self-focusing can prevent the laser pulse from reaching the ideal vacuum intensity. A means to suppress nonlinear propagation before the target is to focus a spatially-chirped pulse: away from focus, the gradually increasing overlap of the spectral components towards the focus leads to simultaneous spatial and temporal focusing, SSTF (Fig 4). The axial localization of intensity offered by this technique has been applied at moderate intensity to nonlinear microscopy and micromachining, where the pulse can be focused through glass or water to the surface to be machined. In previous work, the spatial chirp has been obtained by directing 10's of mJ into a grating-based device that follows the amplifier compressor. In the present work, we send the full uncompressed pulse energy into a single-pass compressor to generate plasma in air with mJ-level pulse energy at 1kHz repetition rate. Although the peak power is  $\sim 1.5$  times the critical power for self-focusing and the intensity is sufficient for strong ionization, we see no evidence for filamentation or ionization defocusing.

A schematic of our experimental set up is shown in Figure 5. A single-pass, folded grating compressor (1200 gr/mm) compressed and spatially chirped the beam. To reduce the thermal load on the first grating, the uncompressed beam was expanded with a curved-mirror telescope. The compressor was nominally at twice the grating separation of our standard double-pass compressor to give a constant group delay across the spectrum for the output pulse. A pair of fold mirrors on a rail allowed for the distance between the gratings to be easily changed, either to adjust the output chirp or to convert to a double-pass arrangement. We focused the output beam with two different configurations: with a spherical mirror ( $f=400\text{mm}$ , elliptical beam aspect ratio 3:1), and an off-axis parabolic mirror ( $f=90\text{mm}$ , beam aspect ratio 4:1). Optimum alignment of the compressor and the beam expander was observed to be critical to achieve the localization of the intensity along the z-axis. The grating surfaces and grooves must be optically parallel, and the input beam divergence must be adjusted so that the individual frequency beamlets focus at the same plane as where the frequency components cross. We used a HeNe alignment laser to set the grating parallelism and inspected the focus of the beam leaving the beam expander to ensure that it was collimated and free of astigmatism. The system transmission was just under 50%. In a system using high-efficiency transmission gratings, built more recently for a different project, we are obtaining approximately 90% transmission.

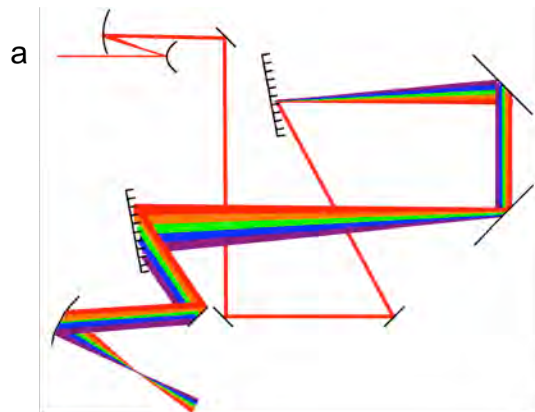


Figure 5. Schematic of the arrangement to focus spatially-chirped pulses. The uncompressed output of the Ti:sapphire amplifier system is directed into the single-pass grating compressor.

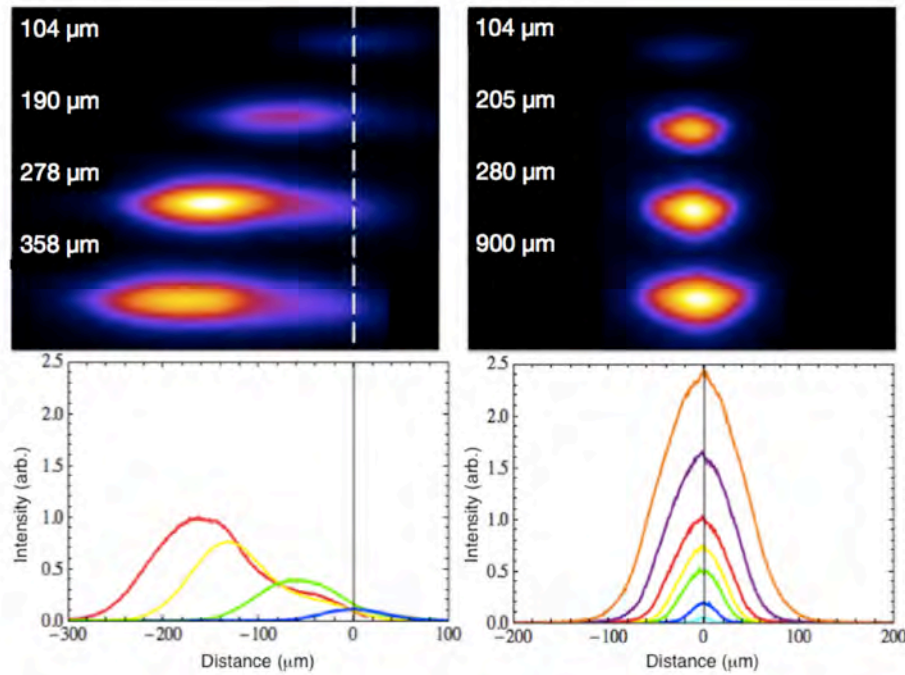


Fig. 6. Image of focus as a function of pulse energy for a standard focal geometry (left) and an SSTF focal geometry (right). The dashed line in the left panel indicates the focal plane of the focusing optic. The beam's focal position shifts toward this focusing optic as the energy is increased.

We made measurements that explicitly demonstrate highly repeatable registration of the focal plane in SSTF. With the standard focusing geometry, self-focusing and ionization defocusing lead to focal plane shifts, focal spot distortion and intensity clamping as a function of the pulse energy. We performed an experiment in which energetic pulses were focused in air to explicitly demonstrate the resistance of SSTF pulses to self-focusing and ionization-induced defocusing (see Figure 6). A 45-degree off-axis parabola (Edmund Optics #83-970),  $f=76.2$  mm, was used to focus 40 fs pulses at 800 nm from a 1 kHz chirped pulse amplification system in air to a 8  $\mu\text{m}$  spot size (FWHM) using both SSTF and conventional (non-SSTF) focusing geometries. The plasma breakdown was imaged from above and recorded as a function of increasing pulse energy. Fig. 6 shows the focal spot intensity profile for a focal geometry without SSTF (left panels). At 104  $\mu\text{J}$  the breakdown is axially symmetric and centered on the focal plane (white dashed line). When the energy is increased to 190  $\mu\text{J}$  the focus has shifted 60  $\mu\text{m}$  toward the parabola, and remains reasonably symmetric. At 278  $\mu\text{J}$ , the focal spot has now shifted by 130  $\mu\text{m}$  and is visibly distorted. By the time the energy reaches 358  $\mu\text{J}$ , the distorted profile has shifted 160  $\mu\text{m}$  away from the focal plane, in a classic self-focusing behavior. Further increasing the pulse energies results in beam filamentation.

With the longer focal length spherical mirror, the size of the spark was easier to resolve spatially. Figure 7a shows a sequence of breakdown emission images taken by a CCD camera with a single lens imaging system. The center image shows the breakdown with no additional

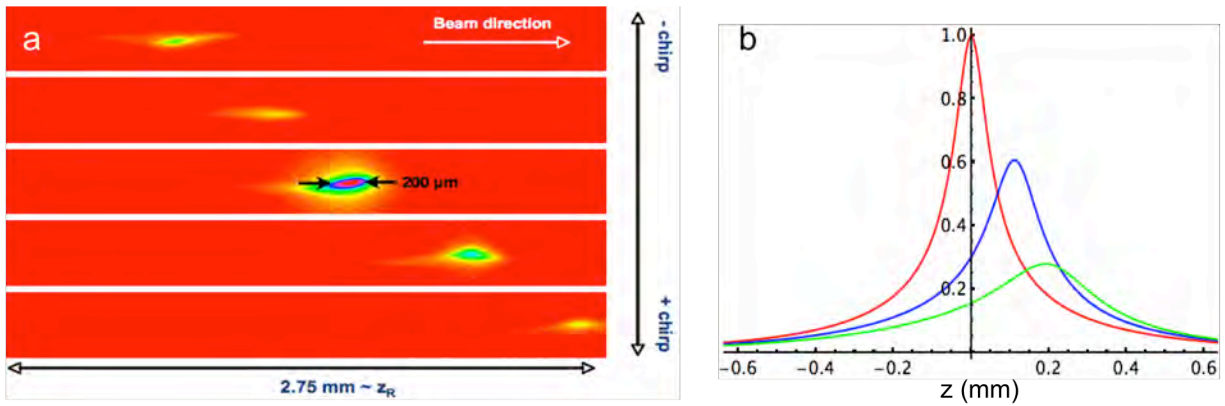


Figure 7. (a) Images of the breakdown plasma for several values of the grating compressor separation. The region of high intensity is observed throughout the Rayleigh range of the beam. (b) Theoretical calculation of change in position and intensity with chirp for a 40fs pulse.

chirp added from the compressor. The spark has a FWHM of 200  $\mu\text{m}$ , 28 times shorter than the confocal parameter of 5.5mm that a non-spatially-chirped beam would have. As seen in microscopy SSTF systems, variation of the input chirp moves the axial position of maximum intensity. Our theoretical analysis shows that the axial localization arises from several contributions: the higher spatial numerical aperture in the chirped direction, the variation of the local bandwidth that determines the minimum pulse duration, and finally, and temporal chirp that varies from positive to negative as the beam passes through focus (as seen in our calculations, Fig 7b). In filamentation studies, input chirp variation can change the location of the filament origin due to compensation of the material dispersion; in this case, the chirp is of geometric origin.

Space-time focusing will find applications where high-intensity pulses that are well above the critical power for self-focusing are to be delivered to a precise location through a medium, as well as to generate high-density plasmas without intensity clamping. Such an application is demonstrated in following section.

### 3. SSTF application: Tissue ablation

As an application and demonstration of the intensity localization of SSTF during this project, we investigated the controlled ablation for biological tissue[3]. The innovation that resulted in the application of femtosecond lasers to micromachining and ophthalmic surgeries was the realization that the damage process went from a statistical to deterministic phenomenon with a well-defined threshold when the pulse duration was scaled from the nanosecond to the femtosecond regime. This has enabled precise surface ablation of a broad range of materials and biological tissues. Despite this precision, in terms of surgical applications there are several key aspects of these systems that confound the potential of femtosecond laser-based tissue ablation. These include the variation in tissue that results in a disparity of ablation thresholds, naturally occurring apertures that limit the numerical aperture (NA) and working distance of the delivery beam, and the location of sensitive membranes that can be within micrometers of the targeted structure(s). The combination of these last two parameters result in a seemingly intractable conundrum, and in fact are further complicated by the real-world realization that pulsed lasers exhibit shot-to-shot energy variation. At low NA and at depth within a tissue, nonlinear effects

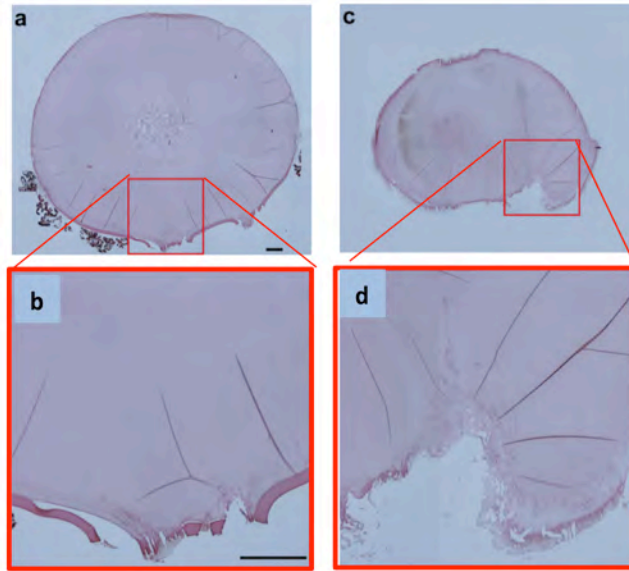


Figure 8. Histology images of cutting of biological tissue (porcine eye lens) with SSTF (a, b) and conventional (c, d) focusing. Lower images are zoomed in sections of the upper images.

such as self-focusing results in focal plane jitter that makes precise cutting up to sensitive boundaries difficult.

In our work, we demonstrated that these issues, which appear intractable, can in fact be addressed through the use of simultaneous spatio-temporal focusing (SSTF). In a SSTF system, as described above, the cutting beam is composed of an angular spectrally sweep of low-NA beamlets that intersect at the focal plane in a single uniform diffraction-limited spot in space, and transform-limited pulse in time. The NA of the beamlets determines the final focal spot size. As a result of the lack of complete spectral overlap in the out-of-focus regions, the peak power and hence intensity of the beam is markedly lower in these zones. The reduced out-of-focus intensity mitigates integrated nonlinear effects such as self-focusing. In our previous work, Vitek et al showed that targeted ablation with 50  $\mu\text{J}$ , 60 fs pulses at 0.05 NA through 6 mm of fused silica was possible with SSTF, while these same beam parameters resulted in filamentation and tracking throughout the solid when a standard focal geometry was used.

Figure 8 shows the histology of the ablated tissues, which were porcine eye samples provided by our collaborators at the University of Colorado Health Sciences Center. The panels left (Figs. 8a,b) show ablation with the SSTF focus, while the panels on the right (Figs. 8c,d) show ablation with a standard focus. The red boxes in the upper row of panels delineate the correspondingly magnified areas shown in the lower panels. From these images it is apparent that the damage only extends to several hundred micrometers for SSTF (panel b) whereas it extends to a millimeter with a standard focus (panel d). Additionally, the localization of the SSTF focal spot directly affects the integrity of the lens capsule, the darker red  $\sim 10 \mu\text{m}$  thick layer of tissue encapsulating the lens. In Fig. 8b the lens capsule remains intact outside of the ablated zone. Notice that various slices of capsule in the SSTF geometry can be seen, marking the rows from sequential passes, separated by 200  $\mu\text{m}$ . Without SSTF, the lens capsule is damaged in regions significantly outside of the ablated zone. Further, we demonstrate that the extension of the ablation zone is axially restricted despite cutting 4 to 58 times above the ablation

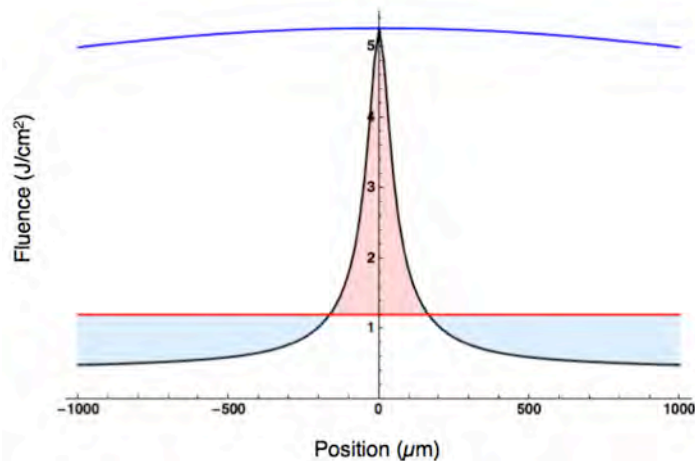


Fig. 9 Fluence as a function of axial position. Blue – is the fluence for the standard focus. Black – is the fluence for the SSTF focus. Red – is the measured ablation threshold (from [13]) for a 100 fs pulse. The light red fill illustrates the portion of the SSTF focus that is above the ablation threshold and the region where damage can be expected. The light blue fill illustrates the region of the SSTF focus below the ablation threshold. Note that the standard focus (blue contour) is above the ablation threshold (red contour) for the entire region depicted in the plot.

threshold. This directly addresses key aspects required for a more intelligent surgical implementation of femtosecond laser pulses. These are, one, the ability to cut with a broad range of fluences without impacting the location of the focal plane which is desirable given tissue differences. Two, the use of beams which have longer working distances facilitating delivery, and three, precise axial ablation with these beams enabling safer penetration up to sensitive boundaries or membranes.

Figure 9 illustrates how the localization of the axial intensity affects ablation (or any threshold process), compared to a conventional focus. The SSTF focus (black) is only above the ablation threshold (red) to a depth of 160  $\mu\text{m}$ , while the standard focus (blue) is above the ablation threshold for millimeters. Figure 9 reinforces precisely what is seen in the histology. The extent of the SSTF ablation should be limited to several hundred micrometers, while the damage with the standard focus should extend to millimeters.

#### ***4. SSTF characterization: Passive dispersion scan, Broadband beamlet scan, and Broadband shearing interferometry***

As seen above, the spatio-temporal structure of beams focused with spatial chirp can lead to a marked advantage over conventional focusing since it allows for energetic beam delivery to a well-defined point in space. These properties, however, depend on good optical alignment of the system. We are developing a more generalized understanding of the propagation of spatially-chirped beams, as well as diagnostics for characterizing the pulses through the focus.

One source of non-ideal behavior is the addition of spectral phase from the laser amplifier system. Fig. 7b illustrates how the axial localization is affected by the addition of second-order phase. There, the axial position of peak intensity shifts because the input spectral phase combines with the geometric phase that results from the evolution of the wavefront curvature of the beamlets through the focus (Fig. 3). With strong third-order phase from the laser system the shift in focal length is not as apparent and the peak intensity and the axial confinement are reduced.

In recent work, we are exploiting the geometric linear chirp that varies through the focal plane to characterize the pulses in situ. When an ultrafast laser pulse is converted to the second harmonic (SH), the spectrum of the SH depends on any extra linear chirp that is applied to the pulse (Fig. 13). Dantus and co-workers have shown that the value of second-order phase that maximizes the SH for a specified spectral position follows the second derivative of the spectral phase. We have demonstrated this effect experimentally, which allows us to optimize the pulse compression without using a delay line for a second pulse or a pulse shaper to control the spectral phase.

Another technique for characterizing SSTF pulses is the spectrally-resolved knife-edge scan (Fig. 11). The knife-edge scan is a standard technique for beam characterization, but in our variation, we spectrally-resolve the power as the edge is scanned across the beam ( $x$ ) for several axial positions ( $z$ ). The power vs  $x$  and  $z$  gives the beamlet direction,  $z$  plane of the beam waist, and the spot size. As a set, we can determine where the beamlets cross. This broadband beamlet scan will give the beamlet axis direction, the location of the waist, and the size of the waist. Since all spectral components of the spatially-chirped beam are scanned at once, this measurement gives the complete description of the spatial characteristics of the spatially-chirped beam.

A third technique that we have recently developed is the spectral shearing interferometer. The superposition of two beams that are transversely sheared (offset in  $x$ ), will result in an interference fringes if the beams are not collimated. For CW beams, an additional crossing angle in the other direction is used to add reference fringes so that the fringes will rotate when the beam diverges. The addition of this crossing angle invariably introduces a time delay, which reduces the fringe contrast for broadband pulses. In our technique, we apply spatially resolved spectral interferometry: we add a time delay without a crossing angle and use fringes in the spectrum as the reference. Fourier analysis gives a very sensitive retrieval of the divergence angle. We are working to extend this to more general self-referenced wavefront measurement.

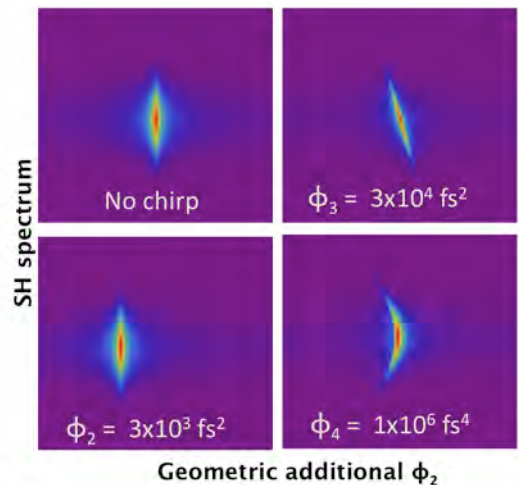


Fig. 10. Calculated variation of the second harmonic (SH) spectrum with addition second order phase. The peak position follows the second derivative of the pulse phase.

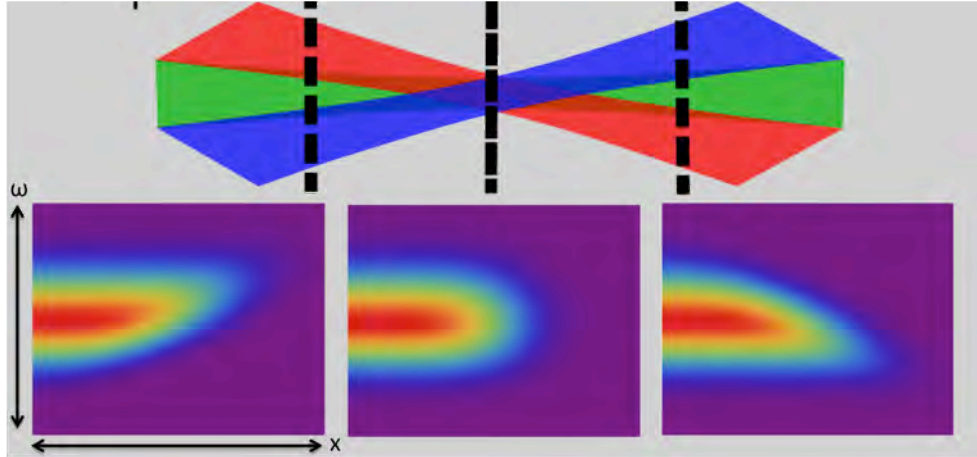


Fig. 11. Top: schematic illustration of a beam with angular spatial chirp passing through a focus. Bottom, calculated spectrum ( $\omega$ ) vs transverse position ( $x$ ) for a knife edge scan at the positions indicated by the dashed lines.

### ***5. Passively stable and dispersion compensated transient grating apparatus to measure ultrafast dynamics***

Femtosecond laser pulse experiments have sufficient temporal resolution to accurately measure ultrafast carrier dynamics through a number of transient pump-probe experiments. To measure carrier dynamics in semiconductor samples and ionizing materials, a novel four-wave mixing (FWM) transient grating (TG) apparatus was developed that is passively stable and dispersion compensated with respect to a reference pulse (see Fig. 12). The TG signal can be used to characterize the input pulse through TG FROG analysis, or through SHG FROG signals generated by the novel apparatus with a slight modification. A CdTe/CdS heterojunction sample was studied using the TG setup by measuring the signal intensity, spectrum, and phase imparted to the signal by the excited lattice in the sample. The phase is extractable using interference between the signal and a reference that passes through an unexcited location of the sample. From three separate measurements of the CdTe/CdS sample, the transient dynamics indicate a short exciton lifetime on the order of several to tens of picoseconds. A high temporal resolution scan reveals a delay of 50 fs between the 3-pulse overlap and the beginning of the lasting response of the sample. Longer temporal range scans and fitting to exponential decay curves indicate fast and slow decay constants. Spectrally, the ultrafast dynamics are non-uniform, which can be attributed to chirped pulses interacting via the instantaneous response of the sample. A TG FROG trace produced in ZnSe confirms the non-uniform spectral structure at early probe delays. The stability found in the phase measurement demonstrates the utility of the apparatus as a phase-sensitive measurement tool, which can be useful for extracting the change in the complex index of refraction due to excitation. We are currently using the techniques developed in this experiment to set up an interferometric probe for plasmas created by intense ultrafast pulses in air as well as to directly scatter probe light from a plasma grating created in air.

## 6. Pulse characterization and energy contrast measurement using crossed-polarized wave generation and self-referenced spectral interferometry

The characterization of degenerate four-wave mixing processes or the interaction of ultrashort pulses with a linearly absorbing material can be sensitive to the energy of a low intensity background. Using spectral interferometry (SI), we interfere the output of a regenerative amplifier with copy of the pulse that has been converted using third-order cross-polarized wave generation (XPW). The amplified spontaneous emission (ASE) background in the pulse shows as a reduced contrast in the interference pattern. The *energy* contrast between the short-pulse and the ASE is retrieved as well as the spectra of the interacting beams. To improve the data analysis we first deconvolve the line spread instrument function of the spectrometer, increasing the fringe contrast of the interference patterns leading to more accurate spectra and better resolution at lower ASE energies.

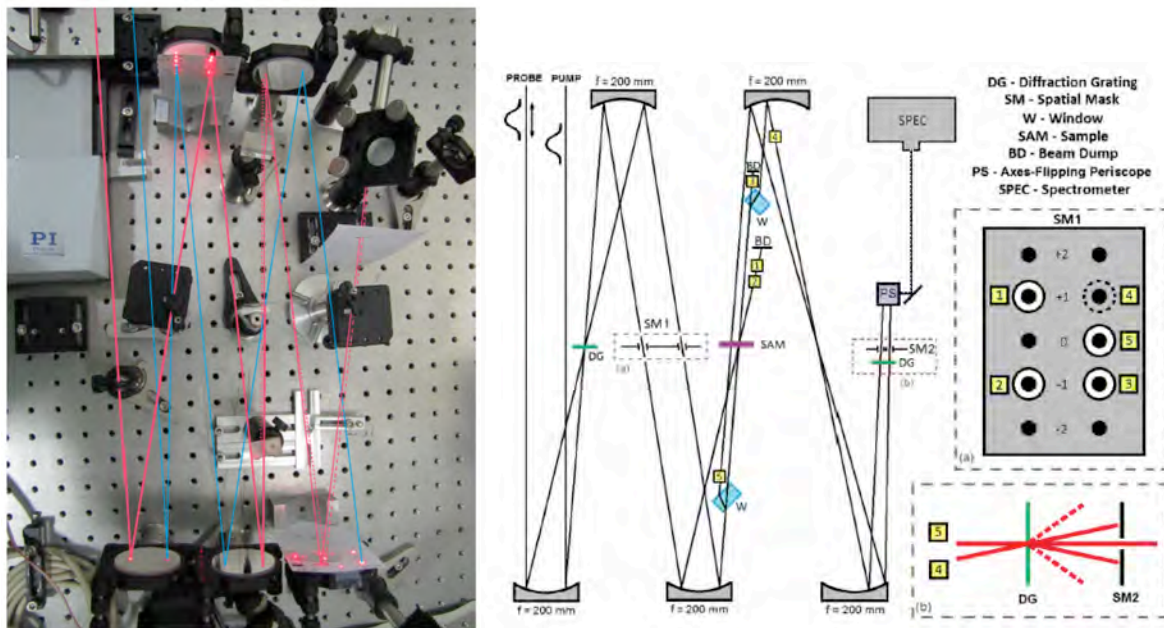


Fig. 12 The TG optical layout used to measure ultrafast transient dynamics. The splitting of the input pulse and the probe delay arm are present before the system seen here.

In chirped-pulse amplification (CPA) systems, amplified spontaneous emission (ASE) results in a long-pulse pedestal on which the compressed short pulse rides. This is particularly an issue for high repetition rate CPA systems that are pumped with either long pulses or continuous wave beams, as well as fiber amplifier systems where the ASE is guided along with the amplified pulses. Figure 13a illustrates the difference between the more commonly measured intensity contrast and the energy contrast. The *intensity* contrast is important for many high-intensity applications, when the pre-pulse can induce *nonlinear* changes in the target before the main pulse arrives. If the target *linearly* absorbs the incident light, the integrated energy in the background can affect the target medium, making a measurement of the *energy* contrast an important parameter. Also sensitive to the energy contrast are degenerate four-wave mixing experiments. For example, the simple measurement of a self-phase modulated spectrum will be

the linear sum of the broadened short pulse spectrum and the spectrum of the long pulse. An incorrect estimate of the energy in the short pulse can lead to errors in characterizing nonlinear response of systems. Having an ASE background can also lead to a mischaracterization of the spectrum of the short pulse, since the seeded spectrum of a laser amplifier is often different than the ASE output. This will result in pulse characterization errors for techniques such as SPIDER that make use of the measured laser spectrum. In laser amplifier chains that are not specifically

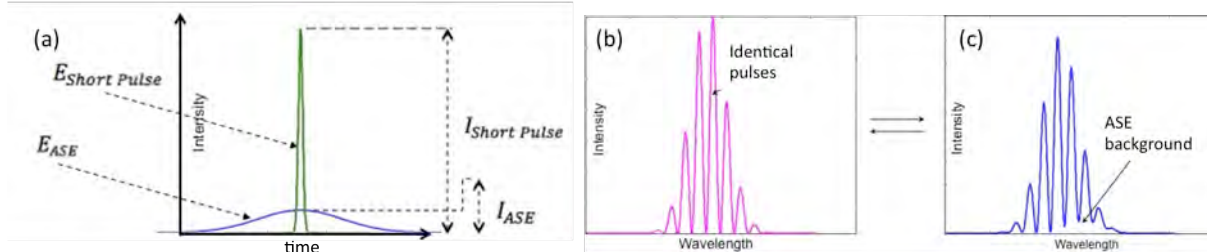


Figure 13. (a) Illustration of short pulse superposed on a long ASE background. (b) High contrast fringes between identical pulses. (c) Reduced fringe contrast when an incoherent ASE background is present.

designed for high intensity contrast (e.g. by inserting nonlinear pulse cleaning devices, an intensity contrast of  $10^6$  might be typical. With this intensity contrast, a regenerative amplifier system that produces a compressed output pulse of 50fs duration and an output pockels cell with a 5 ns window to pass the short pulse and reject the majority of ASE, the fraction of energy in the ASE can be substantial,  $>10\%$ .

In this work, we present a method for using spectral interferometry to measure the energy contrast, as well as the spectrum of the short pulse. We make use of the cross-polarized wave generation (XPW) process, which has been used successfully as a means to dramatically increase the contrast ratio between the peak pulse intensity and the amplified spontaneous emission background of amplifier systems[4]. XPW generation can take place in materials that possess an anisotropic  $\chi^{(3)}$  tensor. The input of an intense, linearly polarized wave generates XPW at the same central wavelength, after which the two pulses are separated with a polarizer[5]. In our arrangement, we use XPW to generate a reference pulse with a dramatically-reduced pedestal content. This XPW pulse is then interfered with the amplifier output pulse. Interference takes place only between the short pulses; the incoherent ASE shows as a background and results in lower fringe contrast. Using Fourier analysis we can recover all the individual spectra and calculate the power under their curves to characterize their energy contrast. Our technique might be considered an add-on to self-referenced spectral interferometry, in which the spectral phase of the short pulse from the amplifier is characterized[6]. Here we are primarily concerned with the characterization of the spectral shapes and energy content.

The model equation for the interferogram is the following:

$$I_{Interference}(\omega) = I_{ShortPulse+ASE}(\omega) + I_{CleanPulse}(\omega) + 2\sqrt{I_{ShortPulse}(\omega) * I_{CleanPulse}(\omega)} \cos(\omega\tau), \quad (13)$$

where  $\tau$  is the delay between the pulses and the  $I(\omega)$ 's represent the intensities of the different input beams. From the earlier discussion, ASE is on a much longer time-scale and is not coherent with the short pulse, so it will not be present in the interference term. The ASE term is present only as a pedestal in the recorded pattern (Fig.13c). It is important to note that a decrease in the fringe contrast can also occur because of mismatched spectral intensity and from the instrument function of the spectrometer.

We tested a Mach-Zehnder setup as well as an inline arrangement shown in Figure 14. This inline setup eliminates the necessity of a delay arm and improves the stability of the experiment results. Our layout is similar in approach to self-referenced spectral interferometry (SRSI) measurement of spectral phase[7]. The output of the laser passes through a BK7 plate set at a Brewster angle to clean up the polarization of the beam and to lower its power to acceptable level for the XPW generation crystal. A calcite plate is used to produce an oppositely polarized, delayed with low energy. The higher-energy pulse is used to create the clean XPW reference pulse (1mm BaF<sub>2</sub>). The delayed pulse, which is polarized in the same direction as the XPW generated pulse, is not substantially affected by the crystal. The relative angle of the first polarizer and the calcite plate are adjusted to give the XPW reference pulse a comparable energy to the delayed pulse. Both pulses are relayed by the 4F imaging system setup to a single slit spectrometer, where the interference pattern is recorded on a camera and analyzed using Fourier transform techniques.

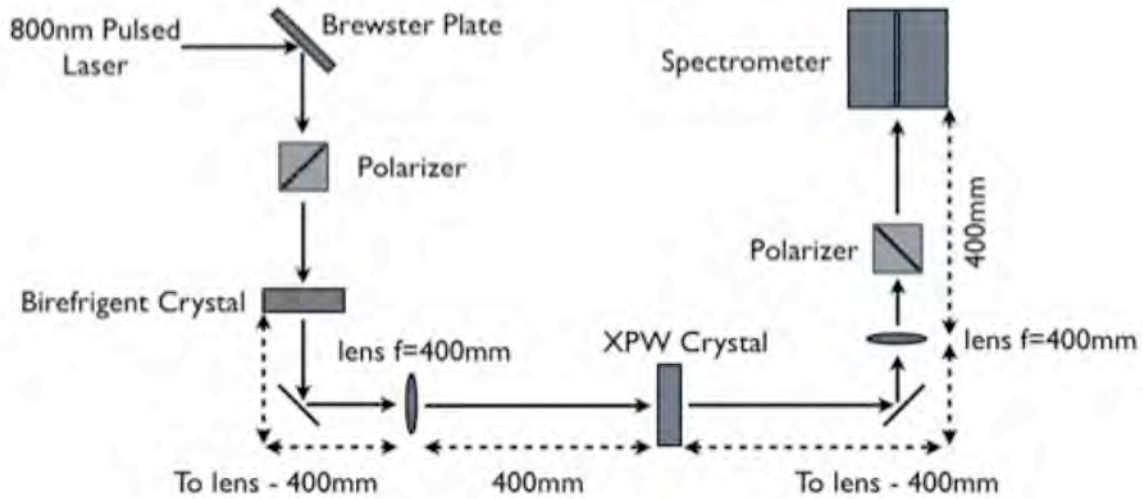


Figure 14. Apparatus to characterize the ASE content of an amplified pulse.

Since the aim is to make use of the balance of the AC and DC components of the interferogram to measure the fraction of the energy that is ASE, it is important to consider the contribution of the imperfect spectrometer resolution to the reduction of contrast of the fringes. Deconvolution of the instrument response for a spectrometer was previously demonstrated by Yetzbacher et al.[8]. This technique, which makes use of a measurement of the lineshape function for a calibration lamp, allows us to remove the effects from a system's impulse response function. Figure 15 shows the raw interferogram and the interferogram after deconvolution.

Figure 16 show representative results from this technique. For a high ASE energy (with the Pockels cell following the regenerative amplifier turned off and the alignment of the seed pulse to the regenerative amplifier slightly detuned) we measure approximately 53% of total energy in the ASE background (Fig. 16, left). The retrieved spectral shapes of the short pulse and ASE are approximately the same in this case. For low energies in the ASE (with the last pulse slicer after the amplifier turned on) we measure 6.6% energy background (Fig. 16, right). This is

approximately the limit of the sensitivity, as can be seen that the spectrum of the background does not have a well-defined shape.

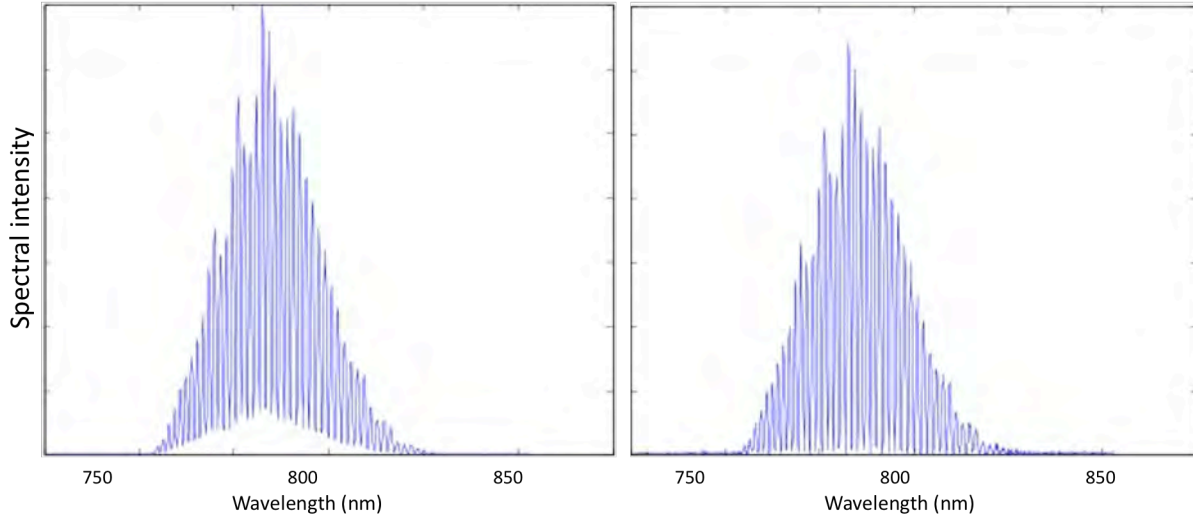


Figure 15. Spectral interferograms. Left: raw data. Right: after deconvolution of the instrument response.

A novel technique for measuring ASE energy in pulse amplifiers has been shown with a simple design, stable operation and the capability of real-time measurement. The energy sensitivity of the approach could be improved by providing a simultaneous measurement of the individual pulse energies. Single-shot collection of the interferogram and reference spectra would also help to decrease the influence of energy fluctuations. The spectral accuracy could be improved by using second-harmonic conversion of a chirped pulse or FROG to separately measure the shape of the short pulse spectrum. We are also exploring a technique to make sure that the retrieved XPW and fundamental spectrum are consistent with the nonlinear generation equations. This will make the ASE retrieval as well as the spectral phase retrieval more robust.

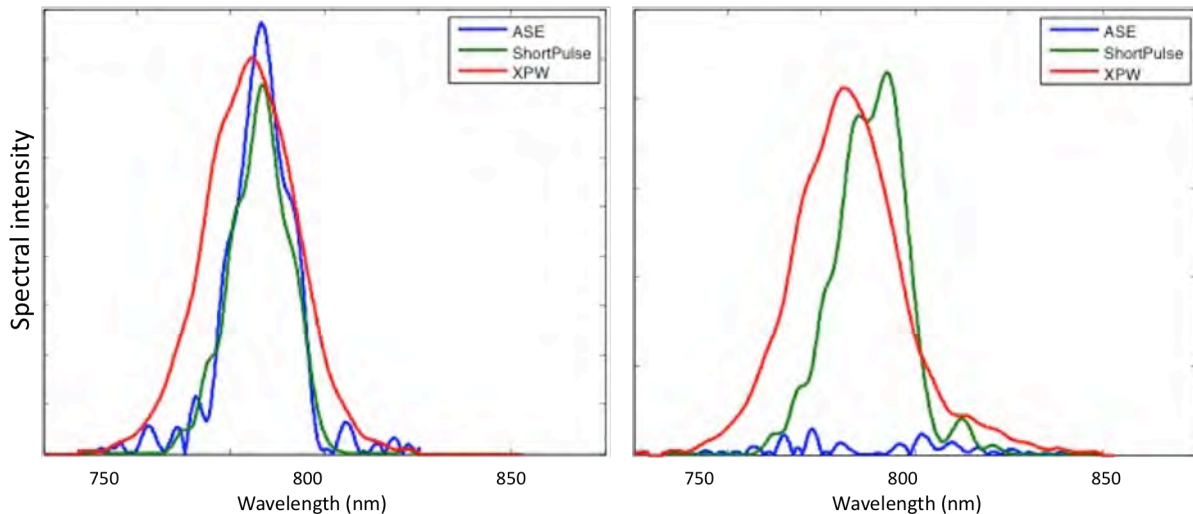


Figure 16. Retrieved XPW (red), short pulse (green) and ASE spectra (blue). Left: Pockels cell after the regenerative amplifier turned off. Right pockels cell turned on to filter the majority of ASE.

## 7. Efficiency Enhancement of Cross-polarized Wave Conversion of Low Energy Pulses via Imaged Double-pass

The efficiency and beam quality of double-pass cross-polarized wave generation is improved by using imaging to better match the two fields for the second pass. The efficiency increase is especially pronounced for low input energy. Cross-polarized wave generation is a degenerate third-order process that produces a new pulse that is proportional to the cube of the input intensity. As such, it can be used to improve pulse intensity contrast by converting only the most intense part of the pulse. The process is sufficiently fast that it can even suppress temporal wings that result from spectral imperfections in compressed wide-bandwidth pulses from gas-filled hollow-core fibers. Conversion efficiencies approaching 25% can be obtained in a single pass for high-energy pulses if the beam profile is very smooth (for example, by passing the beam through a hollow core fiber as a spatial filter). There are some applications where it would be desirable to clean and shorten pulses that have low energy, such as the output of fiber lasers and amplifiers that are often subject to nonlinear distortion and strong amplified spontaneous emission background. The use of a tighter focus or a thicker crystal is limited when the confocal parameter of the beam is smaller than the crystal length. Taking two or more passes can be a way to extend the interaction length at high intensity.

Previous work has shown that the efficiency of the process is substantially improved by using a succession of two crystals compared to a single crystal of the same combined thickness. The fundamental wave (FW) and XPW both converge as they leave the first crystal as a result of the nonlinear lensing in the crystal. Among the factors in the efficiency improvement are the evolution of both the beam sizes and of the relative phase difference between the waves. While the XPW process is not subject to phase-matching in the sense that the  $\text{BaF}_2$  crystal is not birefringent and the process is degenerate, the relative phase between the two fields *is* important if the process is seeded. At the separation that optimizes the conversion efficiency, however, it is observed that the output XPW beam has a ring structure in the far field. The origin of this structure is not yet well understood: two possibilities are that the second-pass XPW has a different size and phase from the first, or that there is a wavefront mismatch across the fundamental and the seed XPW beams that results from their different divergences. In this work we use a curved mirror to relay the pulses from the first pass back to the crystal for a second

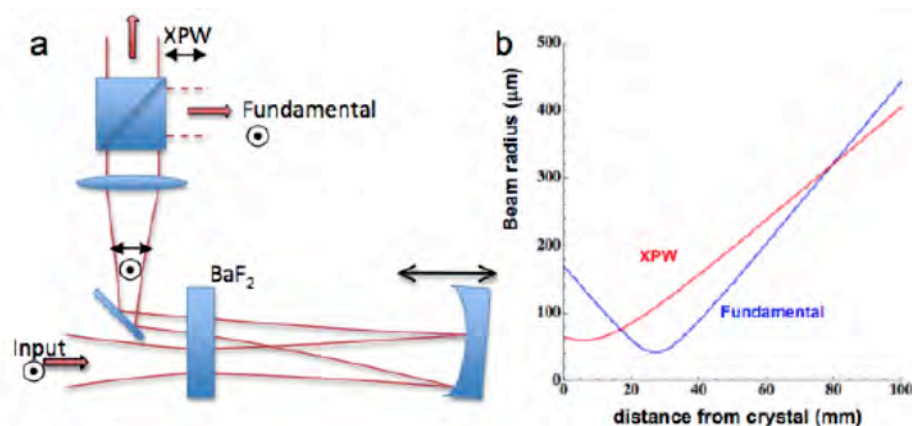


Figure 17. (a) Experiment setup for double-pass XPW generation. (b) Calculated beam size following conversion from the first crystal.

pass. We find that we obtain improved efficiency and better output beam quality (no ring structure). This approach may lead to a scheme for XPW conversion of lower energy pulses over multiple passes.

We focused the compressed output of our Ti:sapphire amplifier system (50fs) with a 100cm focal length mirror into the BaF<sub>2</sub> crystal cut in the 011 orientation. The crystal is placed in a fixed focal plane that optimizes the conversion efficiency. At 20mJ and 50mJ input energy, we obtained 1.5% and 8.5% conversion efficiencies, respectively. The 0.5mm thick crystal is rotated around the z-axis to maximize the XPW signal is strongest. We either used a second crystal with variable separation or reflected the beam back to the first crystal with a variety of focusing mirrors as illustrated in the figure 17. As the crystal-curved mirror separation is

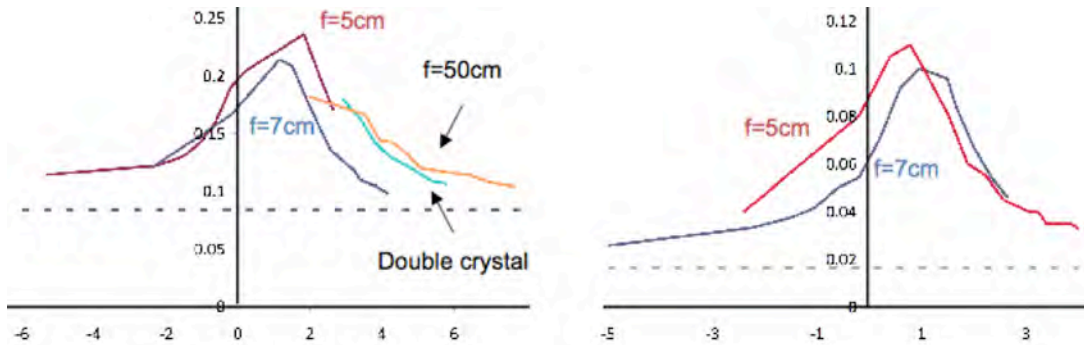


Figure 18. Conversion efficiency vs. crystal separation in cm at the imaging plane. Left: 50μJ, right: 20μJ input energy. Lower dashed line indicates the efficiency from the first pass through the crystal.

increased from the 1:1 imaging position, the fields at the second pass are images of a conjugate plane that is some distance after the first pass. This distance is the effective crystal separation. It is important to note that since a single curved mirror is used to form the image of the fields there is an additional wavefront curvature (not necessarily the same) introduced to the waves. Moreover, while the imaging reproduces the relative beam sizes for the FW and XPW, the amount of magnification will depend on the focal length of the curved mirror.

Figure 18 shows the yield as a function of the effective crystal separation. We first used two separate crystals to establish a reference point. We find similar conversion efficiency with two different crystals and one crystal and f=50cm mirror. We obtain generation of 20% and above for two passes (the proximity of the mounts prevented closer positioning of the two crystals). Imaging with a long focal length mirror, has very little effect on the relayed

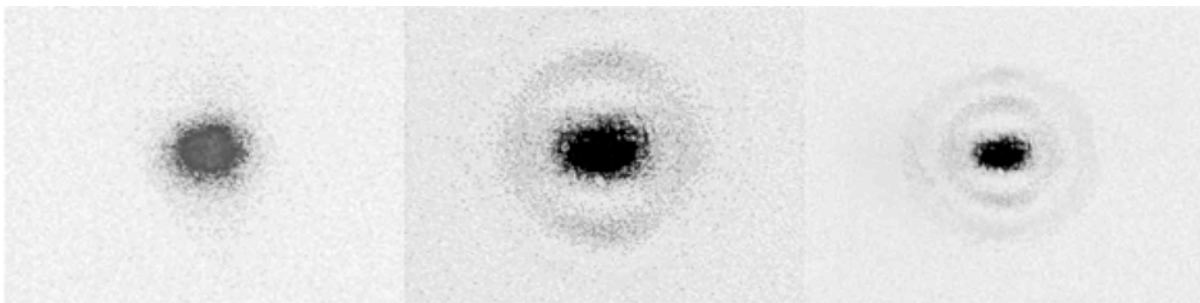


Figure 19. Far-field beam profiles for the XPW beam cross section, from left to right: f= 5cm, 12.8cm, and 50cm imaging mirrors.

magnification and the radii of curvature, and we obtain results similar to the double crystal geometry. In order to establish what conditions are important for the conversion efficiency the focal plane of the crystal is imaged to a camera with a 3x magnification and a spot size radius data was taken at different positions beyond the crystal. We observed that the maximum conversion occurs at  $\sim 2.7\text{cm}$  separation from the original crystal plane or almost where the XPW signal is the smallest in radius. Using the shorter focal length mirrors, we obtain improved conversion efficiency. When the input energy was lowered, giving only 1.5% conversion on the first pass, the improvement in the efficiency on the second pass was dramatically better, reaching a maximum of 11%. We also observed that the ring structure observed with the double crystal and long focal length geometry disappears when the shortest focal length was used (Figure 19). This strongly indicates that the imaging improves the matching of the two waves for the second pass. After modeling the propagation, we plan to extend this concept to multiple passes.

### 8. Pulse delivery to a uniform line focus with shaped Bessel-Gauss beams

Bessel beams have been explored for a number of years as a means to localize the intensity of a laser beam over a distance much longer than the Rayleigh diffraction range corresponding to the focal spot size. Since an ideal conical wave with a constant approach angle to the optical axis will have the same spot size independent of propagation distance, these beams are often called diffraction-free. However, ideal Bessel beams require an infinite amount of energy and thus in practice Bessel beams are realized through truncation of the ideal wave. As illustrated in Figure 20, these apodized Bessel-beams accurately approximate the ideal Bessel beam in a "Bessel-zone" of finite width[9] and transition to a ring-beam in the far field[10], [11].

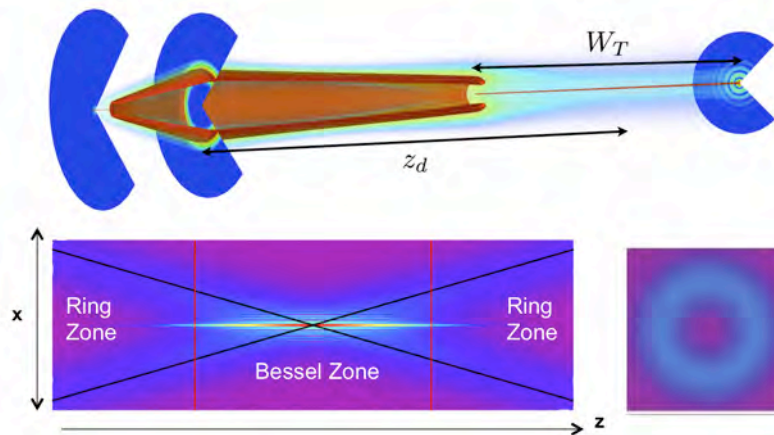


Figure 20. Top: an axicon or a concentric diffraction grating forms a ring beam that is then focused with a lens with focal length  $z_d$ . Bottom: Illustration of the intensity distribution of a Bessel-Gauss beam. The black lines indicate the geometric crossing of the ring beams through the Bessel zone. The red lines show the half-power points of the axial line focus.

There are numerous applications of Bessel beams in a wide range of fields. On low energy systems, Bessel beams have been used for large depth of focus microscopic imaging systems[12], optical tweezers[13], and optical coherence tomography[14]. They also have applications in laser micro-machining[15], laser electron acceleration[16], and filament formation[17]. In addition, to the best of our knowledge, the Bessel beam is the most efficient means of producing a high-intensity line focus, much more efficient than a cylindrical lens focus.

The Bessel-Gauss beams in particular are useful for projecting a line focus to a position at some distance from the optic, especially for intense beams. Of interest to the AFOSR, is a concept of creating a grid of plasma focal lines that could act as a mirror for radar, leading to better relief imaging through a side-looking beam.

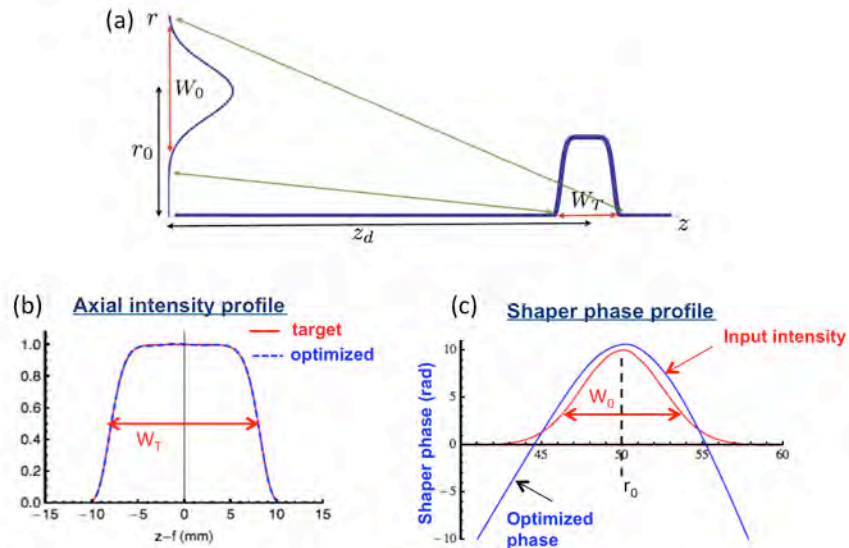


Figure 21. (a) Phase shaping scheme accepts a far-field Bessel-Gauss beam and transforms it to a profile that has a super-Gaussian axial profile. (b) Resulting axial profile fit well to the target intensity profile. (c) The spatial phase for the ring beam (blue) superposed with the input intensity profile (red).

In our work with Bessel-Gauss beams, which was done in a collaboration with the group at U. Arizona, we developed an efficient method for controlling the axial intensity profile of apodized Bessel-beams through a single step of phase-only shaping[18]. Our method is more general than the logarithmic axicon approach in that it allows different initial beam radial profiles to be shaped into a desired on-axis profile. Specifically, we considered starting with a Gaussian ring-beam and adjusting its wavefront to produce a desired axial intensity profile. Such a ring beam can be formed, for example, by passing a Gaussian beam through a diffraction grating with concentric grooves[19]. While both phase and amplitude shaping will perform the task, it is either lossy or requires two separate shaping steps. Our phase shaping scheme is inspired by work that has been performed to shape the focal spot of conventional Gaussian beams. An example is shaping the wavefront of a Gaussian beam to create a super-Gaussian beam profile[20] at the focal plane of a lens. The technique we use in this paper to determine the optimum wavefront is the iterative Gerchberg-Saxton (GS) algorithm[21]. The GS algorithm was originally introduced for phase retrieval in electron microscopes[21] and has since found applications in astronomy [22], radial beam shaping [23], pulse shaping [24] and image reconstruction [25]. While it is well-known that the focal plane of a lens is the Fourier transform of the input field, it is less appreciated that there is a Fourier-like mapping of the input radial profile to the axial profile. This allows us to reduce the two dimensional problem to one. In this work we employ a modified version of the GS algorithm with rapid FFT iteration between two domains to optimize the axial profile to a super-Gaussian. We find that the phase shaping can be simplified by controlling the initial divergence of the input beam before the ring Gaussian is formed.

A key step in devising the shaping algorithm was the recognition that there is an integral relationship between the input radial field profile  $E(r, 0)$  and the on-axis field profile  $E(0, z)$ .

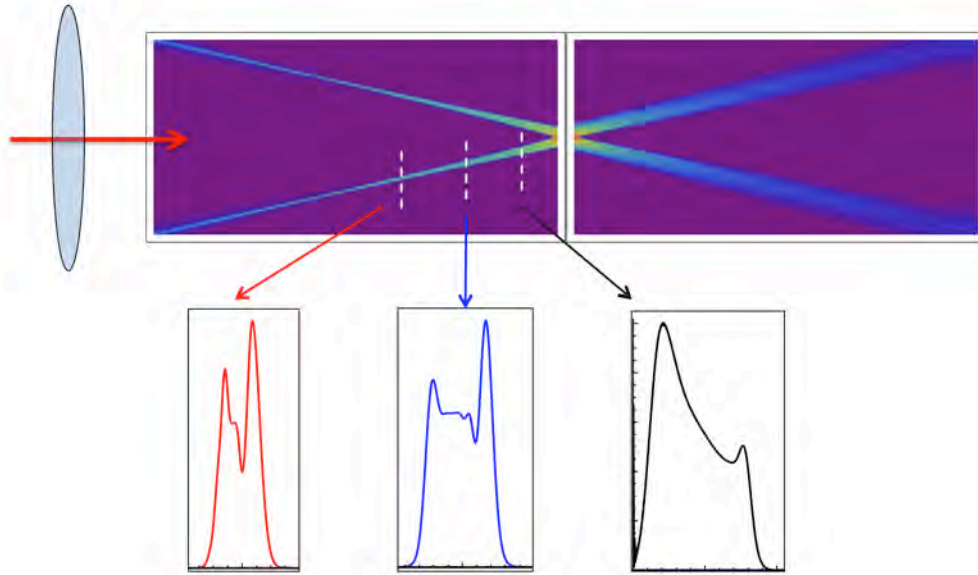


Figure 22. Numerical propagation of the shaped profile for two zones on either side of the lens focal plane. Insets show the radial intensity cross-section of the beam at the axial positions indicated by the dashed lines.

$$E(r=0, z) = i \frac{k_0 A}{2z} \exp[ik_0 z] \int_0^\infty E(s, z=0) \exp\left[i \frac{k_0 s}{2z}\right] ds \quad (14)$$

where the variable  $s = r^2$ . For a ring beam input that is approximately zero on axis, this transform is effectively a Fourier transform with respect to the variable  $s$ . This connection allows rapid iteration for optimization using the Gerchberg-Saxton algorithm.

Representative results are shown in Figure 21, where a ring beam of major radius of 50mm and minor radius of 4mm is focused with a lens of focal length 1m. Without shaping, the axial width is 1.2mm; the target super-Gaussian width is 8mm. The fit is quite good, as seen in Figure 21b. The shaping phase required for this transformation is shown in Figure 8c, and is seen to appear predominantly quadratic in the input plane variable  $(r-r_0)$ .

For flat or random initial radial phase, the GS algorithm did not always converge, stagnating along the way. We approached this issue by providing an initial guess for the phase, using two different approaches. The first approach was based on a recognition that the quadratic portion of the shaper phase shown in Figure 8c is a focusing phase[18]. The second approach was based on a the method of stationary phase applied to the variational problem[26].

Figure 22 shows the evolution of the intensity profile calculated with numerical Fresnel propagation from the input plane with the shaped phase. The ring beam is seen to focus in advance of the focal plane of the lens, where the Bessel zone is located. Thus the role of the focusing term is to extend the length of the axial intensity profile and the higher-order terms of the shaping phase control the fine structure of the shaped beam. The stagnation results in part from the fact that there are two equally valid phase profiles, with positive and negative focusing.

For the purposes of high-intensity beam delivery to a line focus, a negative defocus is preferred to reduce the accumulated  $B$ -integral along the way to the Bessel zone. Using a simple geometric optics initial guess for the required parabolic phase, we were able to obtain good convergence across a wide range of target axial widths (Figure 23). The second approach to obtaining an initial guess was to pose the optimization as a variational problem, then to use the method of stationary phase to analytically obtain an initial guess of the shaper phase.

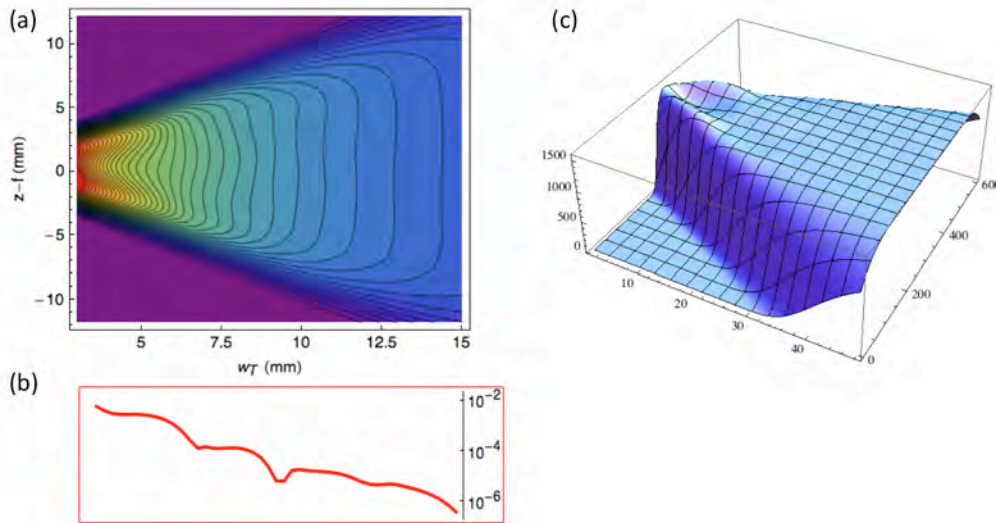


Figure 23. (a) Optimized axial intensity profiles vs target axial width. Profile is closest to a super-Gaussian for larger target widths, as shown in (b), which is the log of the fit error. (c) shows a 3D rendering of (a).

### 10. Direct Diode Pumped Kerr Lens Modelocked Ti:Sapphire Laser Oscillator

An additional project that we pursued during this reporting period was the development of the first Kerr-lens modelocked Ti:sapphire laser directly pumped by laser diodes. This work was published in Optics Express[27] and our summary article was featured on the cover of Laser Focus World[28] (Figure 24). We describe a Ti:sapphire laser pumped directly with 445nm laser diodes. With 44 mW average power at 800 nm and bandwidth for <50 fs pulses, Kerr-lens-modelocked pulses are available with dramatically decreased pump cost. Titanium-doped sapphire is in many respects an excellent gain medium, with an active ion with large bandwidth in a host crystal that is hard and has high thermal conductivity. The high saturation intensity requires laser pumping, typically accomplished with expensive Nd:YVO<sub>4</sub> intracavity doubled pump lasers. Although high-power laser diodes very near the peak absorption at 515nm are not yet available, the recent development of 445 nm high power diodes has opened up the possibility of directly diode-pumping Ti:sapphire oscillators. Current 532 nm pump lasers run ~\$20 k for 3 W, whereas 445 nm diodes are <\$400 for a complete laser package producing 2.2 W, making the motivation for diode-pumping very high. Furthermore, diodes are very simple and robust, which will increase reliability and portability for a new generation of Ti:sapphire laser systems. Recently, work by the University of Strathclyde in Scotland, demonstrated the direct diode pumping of a Ti:sapphire laser oscillator[29], and subsequent modelocking by use of intracavity prisms and a saturable bragg reflector (SBR)[30]. In this work, we report the sustained Kerr lens

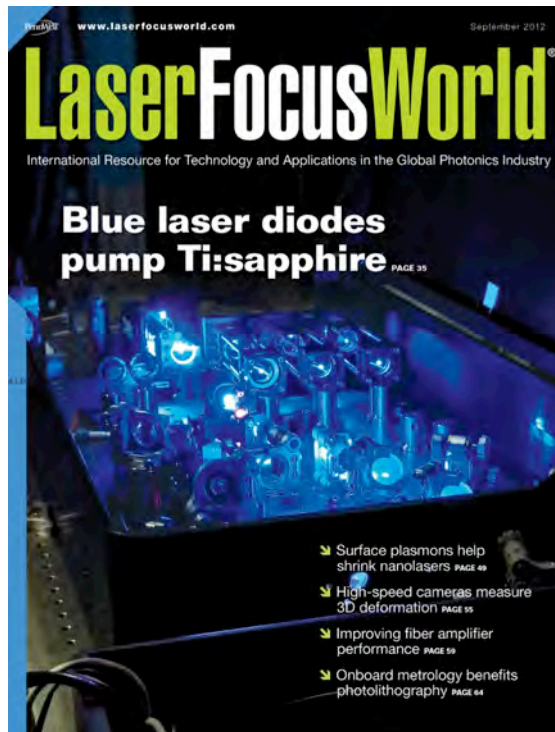


Figure 24. Cover shot from Laser Focus World, featuring our work on direct diode pumping of Ti:sapphire.

modelocking of a Ti:sapphire oscillator using 2.2 W of 445 nm laser diodes and intracavity prisms. In our system, there is no SBR, chirped mirrors, or SESAM.

The layout of the oscillator (Figure 25), which is based on a standard commercial KMLabs oscillator, and is designed to run at low pumping threshold. The oscillator uses a pair of 86 mm ROC mirrors surrounding a 4.75 mm thick Ti:sapphire crystal with an  $a=2 \text{ cm}^{-1}$  at 445 nm, giving 60% absorption of the pump light. The laser is pumped by two 1.2 W 445 nm laser diodes, both of which are collimated by a 6 mm aspheric lens, and a 3:1 cylindrical telescope applied to the slow axis. The pump beams are linearly polarized, and TEC cooled to control the center wavelength and to stabilize the output power. The pump beams are focused with 50 mm

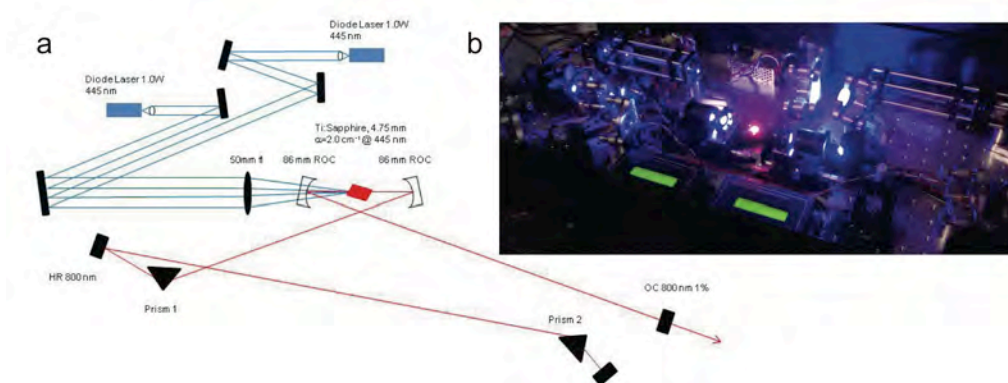


Figure 25. Schematic of directly diode-pumped ultrafast Ti:sapphire oscillator.

lenses onto the Ti:sapphire crystal from both sides. The intracavity prisms for dispersion compensation are fused silica, and are 650 mm apart. The output coupler is 1% at 800 nm. Detuning of the wavelengths help with feedback from one diode into the next. Kerr lens modelocking is initiated by introducing an intensity spike by jogging of one of the prisms. Stable modelocking is demonstrated with a 21 nm spectrum, and an output power of 44 mW maximum (Figure 26). The spectrum supports a 43 fs pulse duration. The pulse train is very stable (Figure 27), and modelocking can be maintained for 15-30 min at a time. The laser will drop out of modelocking due to the air currents on the table, and we anticipate when the laser is housed, stable modelocking will be indefinite.

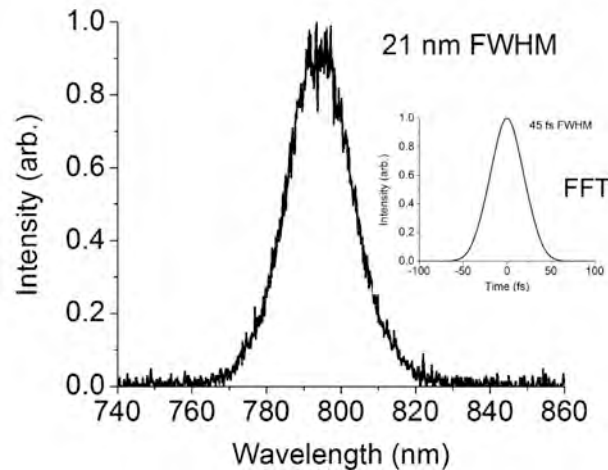


Figure 26. Spectrum of the modelocked pulse train. Inset: Fourier transform of measured spectrum, showing that the bandwidth supports a 43fs pulse width.

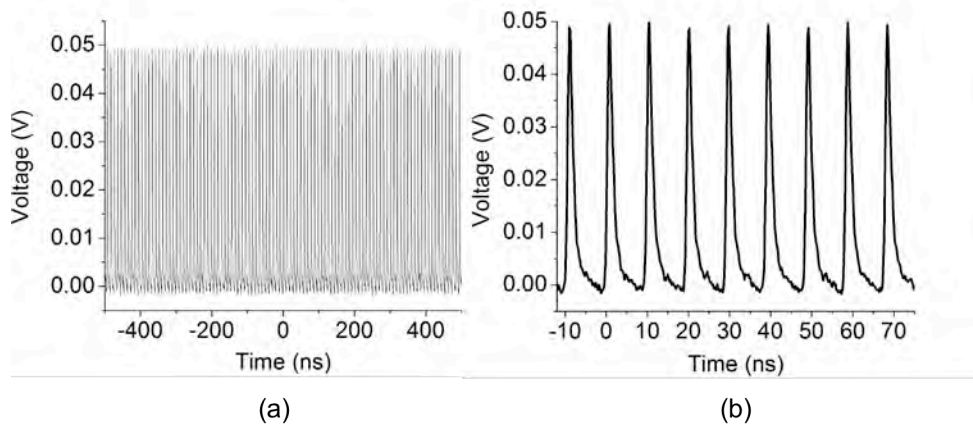


Figure 27. Pulse train of the modelocked output over long (a) and short (b) timescales.

We believe that this is the first demonstration of stable Kerr lens modelocking, by a direct diode pumped Ti:sapphire laser oscillator. In the previous demonstration of modelocking of a Ti:sapphire laser,[30] which required an SBR to sustain modelocking, the authors reported 12mW of average power in a 114fs pulse. We anticipate that with better modematching of the pump beams with the cavity mode, we could increase the output power from 44mW to >100

mW. This work opens the door to much more inexpensive and robust femtosecond oscillator, and the potential for cost effective amplifier systems.

## References:

- [1] C. G. Durfee, M. Greco, E. Block, D. Vitek, and J. A. Squier, "Intuitive analysis of space-time focusing with double-ABCD calculation," *Opt Express*, vol. 20, p. 14244, Jun. 2012.
- [2] C. G. Durfee, M. Greco, E. Block, D. Vitek, and J. A. Squier, "Intuitive Analysis of Ultrafast Pulse Propagation Through Angularly Dispersive Structures," in *New Developments in Photon and Materials Research*, J. I. Jang, Ed. Nova Science Publishers, 2012, pp. 1–26.
- [3] E. Block, M. Greco, D. Vitek, O. Masihzadeh, D. A. Ammar, M. Y. Kahook, N. Mandava, C. Durfee, and J. Squier, "Simultaneous spatial and temporal focusing for tissue ablation," *Biomed. Opt. Express*, vol. 4, no. 6, p. 831, 2013.
- [4] A. Jullien, O. Albert, F. Burgy, G. Hamoniaux, J. P. Rousseau, J. P. Chambaret, F. Augé-Rochereau, G. Chériaux, J. Etchepare, and N. Minkovski, " $10^{-10}$  temporal contrast for femtosecond ultraintense lasers by cross-polarized wave generation," *Opt Lett*, vol. 30, no. 8, pp. 920–922, 2005.
- [5] A. Jullien, O. Albert, G. Chériaux, J. Etchepare, S. Kourtev, N. Minkovski, and S. M. Saltiel, "Nonlinear polarization rotation of elliptical light in cubic crystals, with application to cross-polarized wave generation," *J. Opt. Soc. Am. B*, vol. 22, no. 12, pp. 2635–2641, 2005.
- [6] N. Forget, V. Crozatier, and T. Oksenhendler, "Pulse-measurement techniques using a single amplitude and phase spectral shaper," *J. Opt. Soc. Am. B*, 2010.
- [7] T. Oksenhendler, S. Coudreau, N. Forget, V. Crozatier, S. Grabielle, R. Herzog, O. Gobert, and D. Kaplan, "Self-referenced spectral interferometry," *Appl. Phys. B*, vol. 99, no. 1, pp. 7–12, Feb. 2010.
- [8] M. K. Yetzbacher, T. L. Courtney, W. K. Peters, K. A. Kitney, E. R. Smith, and D. M. Jonas, "Spectral restoration for femtosecond spectral interferometry with attosecond accuracy," *J. Opt. Soc. Am. B*, vol. 27, no. 5, pp. 1104–1117, 2010.
- [9] T. Graf, D. N. Christodoulides, M. S. Mills, J. V. Moloney, S. C. Venkataramani, and E. M. Wright, "Propagation of Gaussian-apodized paraxial beams through first-order optical systems via complex coordinate transforms and ray transfer matrices," *J. Opt. Soc. Am. A*, vol. 29, no. 9, pp. 1860–1869, 2012.
- [10] F. Gori, G. Guattari, and C. Padovani, "Bessel-Gauss beams," *Optics Communications*, vol. 64, no. 6, pp. 491–495, Dec. 1987.
- [11] V. Bagini, F. Frezza, M. Santarsiero, G. Schettini, and G. S. Spagnolo, "Generalized bessel-gauss beams," *Journal of modern Optics*, vol. 43, no. 6, pp. 1155–1166, 1996.
- [12] T. A. Planchon, L. Gao, D. E. Milkie, M. W. Davidson, J. A. Galbraith, C. G. Galbraith, and E. Betzig, "Rapid three-dimensional isotropic imaging of living cells using Bessel beam plane illumination," *Nature Methods*, vol. 8, pp. 417–423, Jan. 2011.
- [13] J. Arlt, V. Garcés-Chávez, W. Sibbett, and K. Dholakia, "Optical micromanipulation using a Bessel light beam," *Optics Communications*, vol. 197, no. 4, pp. 239–245, 2001.
- [14] Z. Ding, H. Ren, Y. Zhao, J. S. Nelson, and Z. Chen, "High-resolution optical coherence tomography over a large depth range with an axicon lens," *Opt Lett*, vol. 27, no. 4, pp. 243–245, 2002.
- [15] F. Courvoisier, J. Zhang, M. K. Bhuyan, M. Jacquot, and J. M. Dudley, "Applications of femtosecond Bessel beams to laser ablation," *Appl. Phys. A*, Sep. 2012.
- [16] B. Hafizi, E. Esarey, and P. Sprangle, "Laser-driven acceleration with Bessel beams," *Phys. Rev. E*, vol. 55, no. 3, pp. 3539–3545, Mar. 1997.
- [17] P. Polynkin, M. Kolesik, A. Roberts, D. Faccio, P. Di Trapani, and J. Moloney, "Generation of extended plasma channels in air using femtosecond Bessel beams," *Opt Express*, vol. 16, no. 20, pp. 15733–15740, Sep. 2008.
- [18] C. G. Durfee, J. Gemmer, and J. V. Moloney, "Phase-only shaping algorithm for Gaussian-apodized Bessel beams," *Opt Express*, vol. 21, no. 13, p. 15777, 2013.
- [19] L. Niggli, T. Lanzl, and M. Maier, "Properties of Bessel beams generated by periodic gratings of circular symmetry," *J. Opt. Soc. Am. A*, vol. 14, no. 1, pp. 27–33, 1997.
- [20] J. A. Hoffnagle and C. M. Jefferson, "Design and performance of a refractive optical system that converts a Gaussian to a flattop beam," *Applied Optics*, vol. 39, no. 30, pp. 5488–5499, 2000.
- [21] R. W. Gerchberg and W. O. Saxton, "Phase determination from image and diffraction plane pictures

- in the electron microscope,” *Optik*, vol. 35, pp. 237–246, Jan. 1972.
- [22] R. A. Gonsalves, “Phase retrieval and diversity in adaptive optics,” *Optical Engineering*, vol. 21, pp. 829–832, Oct. 1982.
- [23] J. S. Liu and M. R. Taghizadeh, “Iterative algorithm for the design of diffractive phase elements for laser beam shaping,” *Opt Lett*, vol. 27, no. 16, p. 1463, 2002.
- [24] A. Rundquist, A. Efimov, and D. H. Reitze, “Pulse shaping with the Gerchberg-Saxton algorithm,” *J. Opt. Soc. Am. B*, vol. 19, no. 10, pp. 2468–2478, 2002.
- [25] J. R. Fienup, “Reconstruction of a complex-valued object from the modulus of its Fourier transform using a support constraint,” *J. Opt. Soc. Am. A*, 1987.
- [26] J. A. Gemmer, S. C. Venkataramani, C. G. Durfee, and J. V. Moloney, “Optical beam shaping and diffraction free waves: a variational approach,” *arXiv.org*, vol. math.OC. 23-Jul-2013.
- [27] C. G. Durfee, T. Storz, J. Garlick, S. Hill, J. A. Squier, M. Kirchner, G. Taft, K. Shea, H. Kapteyn, and M. Murnane, “Direct diode-pumped Kerr-lens mode-locked Ti: sapphire laser,” *Opt Express*, vol. 20, no. 13, pp. 13677–13683, 2012.
- [28] C. Wood, S. Backus, J. Squier, and C. Durfee, “Pumping of Ti:sapphire moves to the blue,” *Laser Focus World*, Sep. 2012.
- [29] P. W. Roth, A. J. Maclean, D. Burns, and A. J. Kemp, “Directly diode-laser-pumped Ti: sapphire laser,” *Opt Lett*, vol. 34, no. 21, pp. 3334–3336, 2009.
- [30] P. W. Roth, A. J. Maclean, D. Burns, and A. J. Kemp, “Direct diode-laser pumping of a mode-locked Ti: sapphire laser,” *Opt Lett*, vol. 36, no. 2, pp. 304–306, 2011.